# Chapter 6
# Hollow Cathodes

Ion and Hall thrusters that utilize an electron discharge to ionize the propellant gas and create the plasma in the thruster require a cathode to emit the electrons. In addition, thrusters must neutralize the ion beam leaving the thruster by providing electrons emitted from a cathode into the beam. The properties of the cathode material, the physical configuration hollow cathode, and structure of the cathode plasma determine, to a large extent, the performance and life of both ion and Hall thrusters.

## 6.1 Introduction

Early electron-bombardment ion thrusters developed in the 1960s utilized directly heated tungsten filaments as the cathode that produced electrons for the plasma discharge. Smaller tungsten filaments were also inserted into the ion beam to provide neutralizing electrons. Due to the high work function of tungsten, these filaments had to be operated at temperatures of over 2600 K in order to emit electron current densities in excess of 1 A/cm$^2$. Operation at these temperatures requires high heater power, often on the order of the discharge power, which significantly reduces the efficiency of the thruster. In addition, the life of filament cathodes is limited by rapid evaporation of the filament material at the elevated temperatures and by sputtering of the tungsten surface exposed to the discharge plasma or the beam by ion bombardment. Filament cathode life was typically limited to the order of only hundreds of hours or less. While the use of filament cathodes permitted development of ion thruster accelerator grids and discharge chambers, they were inadequate for long-life space applications.

These problems were solved by the development of hollow cathodes. A generic hollow cathode is shown in Fig. 6-1, where the cathode consists of a hollow refractory tube with an orifice plate on the downstream end. The tube has an insert in the shape of a cylinder that is placed inside the tube and pushed against

the orifice plate. This insert is the active electron emitter, and it can be made of several different materials that provide a low work function surface on the inside diameter in contact with the cathode plasma. The cathode tube is wrapped with a heater (a co-axial sheathed heater is shown in the figure) that raises the insert temperature to emissive temperatures to start the discharge. The electrons emitted from the insert ionize gas injected through the cathode tube and form a cathode plasma from which the discharge-current electrons are extracted through the orifice into the thruster plasma.

A hollow cathode can be separated into three distinct plasma regions illustrated in Fig. 6-2: a dense plasma in the insert region interior to the cathode, a high current density plasma in the orifice, and a diffuse plume plasma outside of the cathode that connects to the thruster discharge plasma. The plasma ions generated throughout the device neutralize the electron space charge; as a result, hollow cathodes produce high currents at low voltages as compared with vacuum cathode devices.
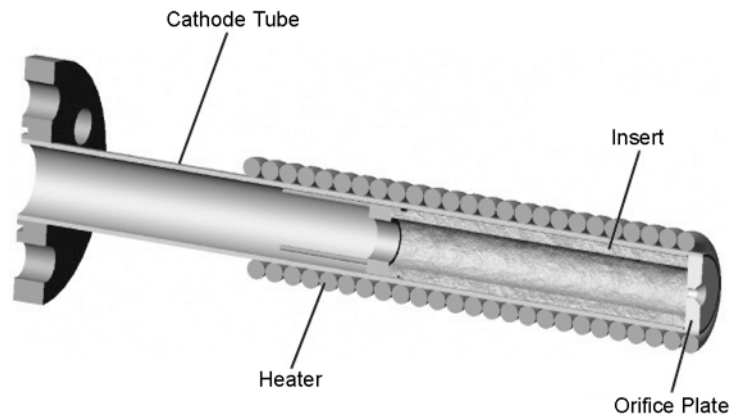


**Fig. 6-1. Typical hollow cathode geometry of a refractory metal tube with an emissive insert inside and a heater wrapped on the outside.**
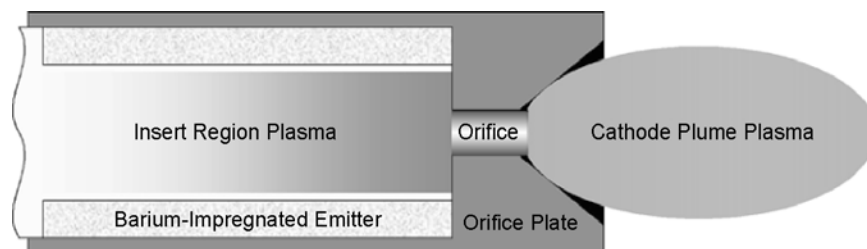


**Fig. 6-2. The three plasma regions in a hollow cathode.**

The structure of the hollow cathode serves three main functions. First, some fraction of the thruster propellant is injected through the hollow cathode, and the discharge inside the resulting high neutral pressure region generates a cold, high-density plasma. The plasma and neutral densities are the highest of anywhere in the thruster, and the electron temperature is correspondingly the lowest. This causes the plasma potential inside the hollow cathode to be very low, reducing the energy of the ions that arrive at the insert surface. This characteristic behavior is demonstrated in Fig. 6-3, which shows the measured potential and density profiles in the Nuclear Electric Xenon Ion Thruster System (NEXIS) hollow cathode [1] discharge. Plasma densities in excess of $10^{14}$ cm$^{-3}$ are routinely generated inside hollow cathodes, and the electron temperature is found [2] to be only 1 to 2 eV. The low plasma potential in the insert region and high neutral scattering rates decrease the ion bombardment energy striking the insert surface to typically less than 20 eV, which essentially eliminates ion sputtering of the surface and greatly increases the life of the cathode. Second, the high-density plasma in the insert region eliminates space charge effects at the cathode surface that can limit the electron emission current density. Emission current densities of 1 to 10 A/cm$^2$ are typically employed in thruster hollow cathodes for compact size and good life, although higher
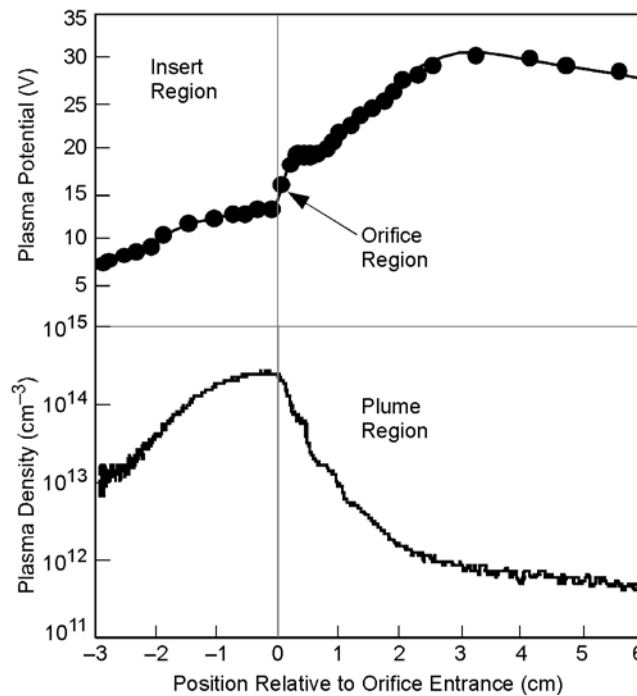


**Fig. 6-3. Plasma potential (top) and density (bottom) measured on axis in the NEXIS hollow cathode at 25 A of discharge current.**

current densities are achievable and sometimes used. Third, the cathode insert can be heat shielded well in this geometry, which greatly reduces the radiation losses of the cathode at operating temperatures. This decreases the amount of power that must be deposited in the cathode to maintain the required temperature for electron emission. This reduces the cathode heating losses to a small fraction of the discharge power, significantly reducing the discharge loss of the plasma generator.

Since nearly the entire discharge current runs through the orifice, the current density there is highest in the system, and a sufficient plasma density must be generated locally to carry the current. For the 25-A discharge case shown in Fig. 6-3, the plasma density in the orifice is on the order of $10^{14}$ cm$^{-3}$. The discharge current flowing through the 2.5-mm-diameter orifice is described by

$$I = n_e evA ,\qquad\qquad (6.1\text{-}1)$$

where $n_e$ is the plasma density, $e$ is the electron charge, $v$ is the electron drift velocity, and $A$ is the cross-sectional area of the orifice. Solving for the drift velocity gives

$$v = \frac{I}{n_e eA} = 7.7 \times 10^4 \ \text{m/s} \ \ll v_{th} ,\qquad\qquad (6.1\text{-}2)$$

where the thermal drift velocity $v_{th} = \sqrt{kT_e / m}$ is $6 \times 10^5$ m/s for the 2-eV plasma electron temperatures measured in this location. The current is conducted through the orifice region at relatively low drift velocities, even though the electron current density exceeds 100 A/cm$^2$ in this case. This is typically true even at current densities exceeding 1000 A/cm$^2$.

In the plume region, the expanding orifice plasma and ionization of the expanding neutral gas provide an ion background that neutralizes the space charge of the current carrying electrons. Hollow cathodes are normally enclosed in another electrode called a keeper, shown in Fig. 6-4. The major functions of the keeper electrode are to facilitate turning on the cathode discharge, to maintain the cathode temperature and operation in the event that the discharge or beam current is interrupted temporarily, and to protect the cathode orifice plate and external heater from high-energy ion bombardment that might limit the cathode life. The keeper is normally biased positive relative to the cathode, which either initiates the discharge during start-up or reduces the ion bombardment energy during normal operation. The life of the keeper electrode is very important to the life of the cathode and thruster.
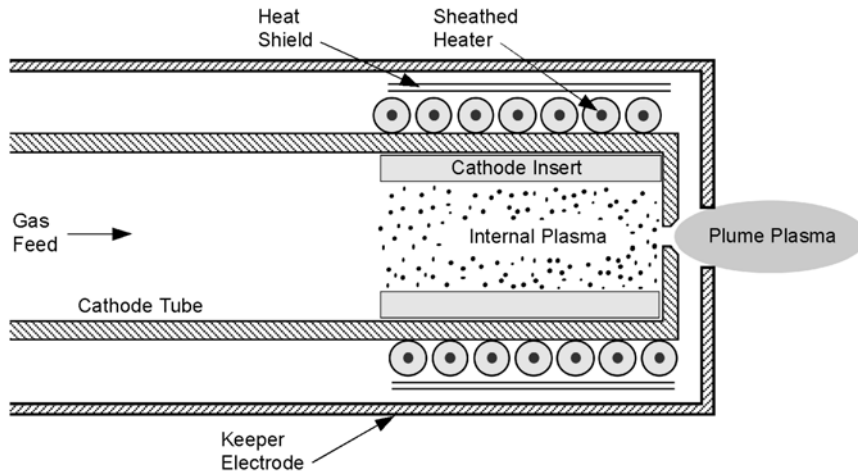
**Fig. 6-4. Hollow cathode schematic showing the cathode tube, insert, and heater enclosed in a keeper electrode.**

Hollow cathodes operate in a "self-heating" mode, in which the external heater is turned off during operation and the cathode insert is heated by plasma bombardment. There are three self-heating mechanisms possible in hollow cathodes: (1) orifice heating, (2) ion heating, and (3) electron heating. In orifice heating, the cathode is designed with a small, restrictive orifice, which produces a high internal pressure in both the insert and orifice regions. The plasma discharge passing through the orifice is then very resistive, causing a significant amount of power to be deposited in the orifice plasma and transferred to the orifice walls by convection. This power deposition then heats the insert by conduction and radiation. Orifice heating is used primarily in neutralizer cathodes where the discharge currents are very low. The classic mechanism for cathode heating is ion heating, where ions in the cathode insert region plasma fall through the sheath potential at the insert surface and heat the surface by ion bombardment. Electron heating occurs in a regime where both the cathode internal pressure and the discharge current are relatively high, resulting in the very high plasma densities ($>10^{15}$ cm$^{-3}$) generated in the insert region. The low electron temperatures and low sheath voltages produced in this situation result in the energetic tail of the Maxwellian electron distribution having sufficient energy to exceed the sheath potential and reach the insert surface. These electrons then deposit their energy on the insert and heat it to emission temperatures. The heating mechanism that dominates in any hollow cathode design depends on the geometry of the cathode, the internal neutral gas pressure in the insert and orifice regions, and the discharge current.

This chapter will start with a simple classification of different hollow cathode geometries to aid in the discussion of the important effects in the system, and

then discuss the basics of the cathode insert that provides thermionic electron emission. The characteristics of the plasmas in the insert region, the orifice, and the cathode plume in the vicinity of the keeper required to extract and transmit the electrons into the thruster will then be examined. Since the neutral gas density changes all along the discharge path in hollow cathode discharges, the plasmas generated in each location (inside the insert, in the orifice, and in the cathode plume) have different properties in terms of collisionality, temperature, potential, and density. These differences determine the applicable plasma physics in each region.

## 6.2  Cathode Configurations

The geometry and size of the hollow cathodes depend on the amount of current that they are required to emit. Discharge currents in ion thrusters are typically 5 to 10 times the beam current depending on the efficiency of the plasma generator, and discharge currents can range from a few amperes to over 100 amperes [3]. The hollow cathode used in a Hall thruster provides electrons for both ionization of the propellant gas and neutralization of the beam [4]. Hall thrusters also tend to run at lower specific impulse (Isp) than ion thrusters. Therefore, Hall thrusters require higher discharge currents from the cathode to achieve the same total power as compared to ion thrusters, and currents of the order of 10 amperes to hundreds of amperes are needed. Neutralizer cathodes in ion thrusters emit electrons at a current equal to the beam current. Therefore, they can be made smaller than discharge cathodes and must be designed to be self-heated and to run reliably at lower currents.

Higher discharge currents require larger insert sizes because the thermionic emission current densities from cathode surfaces are finite. Ultimately, this determines the diameter of the insert, which will be described in the next section. The cathode orifice size depends on many parameters. Ion thruster neutralizer cathodes have been designed with very small diameter orifices ($\leq 3 \times 10^{-2}$ cm), and ion thruster discharge cathodes and small Hall thruster cathodes have been designed with orifices of less than 0.1-cm diameter to over 0.3 cm in diameter. High-current hollow cathodes for large ion thrusters and Hall thrusters will have even larger orifices. These cathodes are sometimes designed even without an orifice, where the insert inside diameter forms a tube exposed to the discharge plasma.

Hollow cathodes generally fall into three categories, which will be useful later in describing the plasma characteristics in the three regions described above. The first type of hollow cathode is characterized by a small orifice with a large length-to-diameter ratio, shown schematically in Fig. 6-5 as Type A. These cathodes typically operate at low current and relatively high internal gas
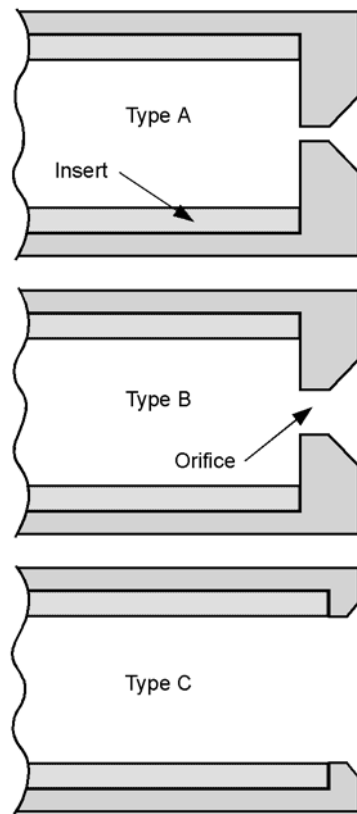
**Fig. 6-5. Schematics of the three characteristic types of hollow cathodes (A, B, and C) depending on the orifice geometry.**

pressures, and are heated primarily by orifice heating. The second type of cathode features has an orifice diameter typically larger than the length, shown in Fig. 6-5 as Type B, and operates at lower internal gas pressures. The heating mechanism in these cathodes can be due to electron or ion bombardment of the insert, or a combination of the two depending on the orifice size and operating conditions. The third type of cathode, typically used in high-current cathodes and shown in Fig. 6-5 as Type C, has essentially no orifice at all. These cathodes have a large neutral density gradient in the insert region, but they typically have a reduced internal pressure overall as compared to orificed cathodes. The heating mechanism for Type C cathodes is normally ion bombardment of the insert.

The value of the neutral gas pressure inside the hollow cathode affects both the plasma density and plasma profile due to collisional effects [5]. Figure 6-6 shows examples of axial plasma density profiles measured with fast scanning probes [6] inside a 0.38-cm inside-diameter (I.D.) cathode insert operating at 13 A of discharge current and a xenon flow of 3.7 standard cubic centimeters per minute (sccm) for two different orifice diameters and the case of no orifice plate at all. Small orifices, characteristic of Type A cathodes, have high internal pressures that produce high plasma densities but constrain the axial extent of the plasma to the order of a few millimeters. For a given emission current density, this can restrict the discharge current that is available. As the orifice is enlarged, the pressure decreases and the plasma extends farther into the insert, resulting in utilization of more of the insert surface area for electron emission.

The electron current density in the orifice is higher than anywhere else in the system and, depending on the orifice size, can easily exceed 1 kA/cm$^2$. If the orifice is long compared with its radius, as is the case in most Type A neutralizer hollow cathodes, the physics are the same as for a classical positive
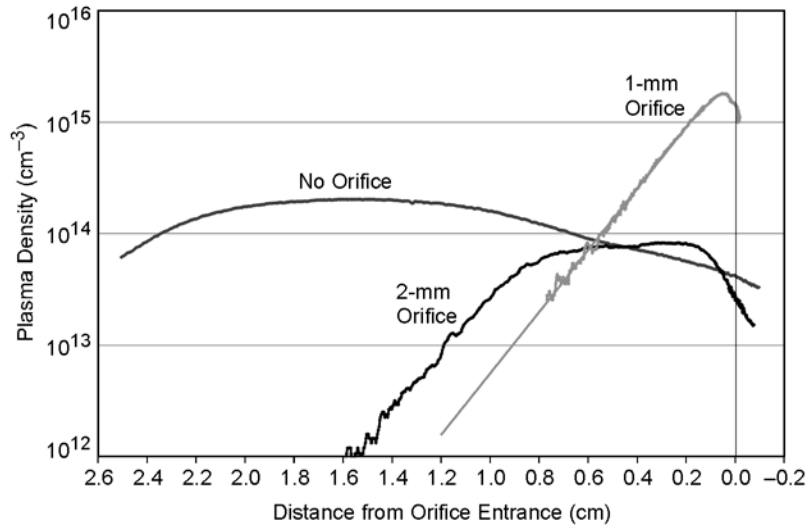
**Fig. 6-6. Cathode plasma density profile examples as the orifice diameter is increased for a constant discharge current and flow rate.**

column plasma where an axial electric field in the collisional plasma conducts the current and plasma resistive heating is very important. A large fraction of this ohmic power deposited in the orifice plasma goes into heating of the orifice plate by ion bombardment, which contributes to the insert heating by conduction and radiation. In Type B cathodes, the orifice is shaped nearly as an aperture, and there is little local resistive heating. The plasma in the insert region is generated by ionization of the neutral gas by the discharge current flowing through the insert region into the orifice. At high cathode neutral-gas flows (and subsequent high plasma density) in this type of cathode, the insert heating is primarily by plasma electrons. At low flow rates or with large orifices, the insert is heated predominately by the ions bombarding the emitter surface. In Type C cathodes, there is little or no orifice, and the plasma couples from a collisionally dominated region upstream inside the insert directly into the nearly collisionless cathode plume region. This creates long axial density and potential gradients and may expose some of the downstream region of the insert to higher potentials and ion bombardment. Heating in this case is predominately by ion bombardment through the higher cathode sheath potential.

Naturally, there is a continuous range of cathode operation that may demonstrate properties of all three cathode types. Indeed, a given cathode geometry can transition from low resistive heating in the orifice at low currents and low gas flow rates to substantial resistive heating and plasma generation at high currents and high gas flow rates. These three types of hollow cathodes will

be discussed in detail after the actual thermionic electron emitter properties are described.

## 6.3 Thermionic Electron Emitter Characteristics

Electrons are introduced into the system by thermionic emission from the insert surface. Thermionic emission by cathodes is described by the Richardson–Dushman equation [7]:

$$J = A \, T^2 \, e^{-e\phi/kT} \, , \qquad (6.3\text{-}1)$$

where $A$ is, ideally, a constant with a value of 120 A/cm$^2$K$^2$, $T$ is the temperature in kelvins, $e$ is the charge, $k$ is Boltzmann's constant, and $\phi$ is the work function. Experimental investigations of the thermionic emission of different materials reported values of $A$ that vary considerably from the theoretical value. The cause of the deviation of $A$ from a constant has been attributed to several different effects, such as variations in the crystal structure of the surface, variations in the surface coverage (for dispenser cathodes), changes in the density of states at the surface due to thermal expansion, etc. This issue has been handled [8] for many of the thermionic electron emitters used in hollow cathodes by introducing a temperature correction for the work function of the form

$$\phi = \phi_o + \alpha T \, , \qquad (6.3\text{-}2)$$

where $\phi_o$ is the classically reported work function and $\alpha$ is an experimentally measured constant. This dependence can be inserted into Eq. (6.3-1) to give

$$J = Ae^{-e\alpha/k}T^2 \, e^{-e\phi_o/kT} = D \, T^2 \, e^{-e\phi_o/kT} \, , \qquad (6.3\text{-}3)$$

where $D$ is a material-specific modification to the Richardson–Dushman equation.

In the presence of strong electric fields at the surface of the cathode, the potential barrier that must be overcome by the electrons in the material's conduction band is reduced, which results effectively in a reduced work function. This effect was first analyzed by Schottky [9], and the so-called Schottky effect is included in the emission equation by the addition of a term [10] to describe the effect of the surface electric field on the emission current density:

$$J = D \, T^2 \, \exp\left(\frac{-e\phi_o}{kT}\right) \exp\left[\left(\frac{e}{kT}\right)\sqrt{\frac{eE}{4\pi\varepsilon_o}}\right], \qquad (6.3\text{-}4)$$

where $E$ is the electric field at the cathode surface. The Schottky effect often becomes significant inside hollow cathodes where the plasma density is very high and the electric field in the sheath becomes significant.

The properties of the material selected for the thermionic emitter or insert determine the required operating temperature of the cathode for a given emission current. The work functions and values of $D$ found in the literature for several common cathode materials are summarized in Table 6-1. Figure 6-7 shows the emission current density calculated using Eq. (6.3-3) for several different emitter materials. The refractory metals are seen to have work functions in excess of 4 eV, and so they must operate at very high temperatures to achieve significant emission current density.

The so-called "oxide" cathodes have work functions under about 2 eV and so are capable of producing high emission current densities at temperatures under 1000°C. Oxide layers, such as barium oxide, were first deposited on tungsten or nickel filaments to lower the work function and reduce the heater power required. However, these surface layers evaporate and are easily sputtered by ion bombardment, limiting the life in vacuum applications to thousands of hours and in plasma discharges to tens of hours. This problem was mitigated by the development of dispenser cathodes where a reservoir of the oxide material is fabricated into the tungsten substrate, which continuously re-supplies the low work function surface layer. The most commonly used dispenser cathode in thrusters, the "Phillips Type S," uses a porous tungsten matrix that is impregnated with an emissive mix of barium and calcium oxides and alumina [16]. Different molar concentrations of the three constituents of the emissive

**Table 6-1. Work function and Richardson coefficients for several cathode materials.**

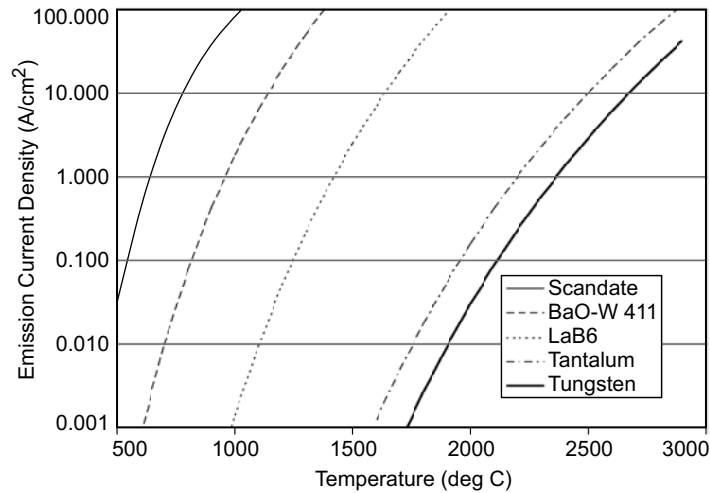|                     | $A$   | $D$   | $\phi$                                              |
|---------------------|-------|-------|-----------------------------------------------------|
| BaO-Scandate [11]   | 120   | —     | $8 \times 10^{-7} T^2 - 1.3 \times 10^3 T + 1.96$   |
| BaO-W 411 [12]      | 120   | —     | $1.67 + 2.82 - 10^{-4} T$                           |
| BaO-W 411 [10]      | —     | 1.5   | 1.56                                                |
| LaB$_6$ [13]        | —     | 29    | 2.66                                                |
| LaB$_6$ [14]        | —     | 110   | 2.87                                                |
| LaB$_6$ [15]        | 120   | —     | 2.91                                                |
| LaB$_6$ [8]         | 120   | —     | $2.66 + 1.23 \times 10^{-4} T$                      |
| Molybdenum [8]      | —     | 55    | 4.2                                                 |
| Tantalum [8]        | —     | 37    | 4.1                                                 |
| Tungsten [8]        | —     | 70    | 4.55                                                |

**Fig. 6-7. Emission current density versus temperature for various cathode materials.**

mix are used depending on the required emission current density and life. In ion thrusters, a 4:1:1 emissive mix typically is used, although other mixtures are available [1]. The matrix material containing the impregnate can be directly heated by passing a current through the material, or configured as an insert placed inside hollow cathodes.

In dispenser cathodes, chemical reactions in the pores of the matrix or at the surface at high temperatures reduce the emissive material and evolve a barium-oxide dipole attached to an active site on the tungsten substrate. The 4:1:1 Type S cathode has a work function of about 2.06 eV at temperatures in excess of about 800°C. Barium-oxide dispenser cathodes with porous matrix material made of tungsten can provide emission current densities of 10 A/cm$^2$ at surface temperatures of about 1000°C, as shown in Fig. 6-7. The work function can be further reduced by the introduction of small amounts of other refractory materials, such as iridium or osmium, in the tungsten matrix. These "mixed metal matrix" cathodes can have work functions below 1.9 eV, and they typically slow some of the chemical reactions that take place in the cathode. It was also found that the addition of scandium to the surface of the barium-oxide dispenser cathode reduces the work function significantly. This is reflected in Fig. 6-7, where the reported work function [11] at 1100°C is about 1.7 eV, which is significantly less than the 2.06 eV for the BaO dispenser cathode and results in much lower temperatures for a given emission current density. The mechanism for this improvement is not clear to date, and the ability to fabricate stable scandate electron emitters that maintain the low work function over time

has been problematic. However, scandate–BaO–W dispenser cathodes have been successful in several different cathode structures.

Because chemistry is involved in the formation of the low work function surface, dispenser cathodes are subject to poisoning that can significantly increase the work function [17]. Some care must be taken in handling the inserts and in the vacuum conditions used during operation of these cathodes to avoid poisoning by impurities in the gas that produce unreliable emission and shorten the lifetime. In addition, impurities in the feed gas that react with the tungsten insert can cause migration and deposition of tungsten or tungstates (compounds of tungsten, barium, and oxygen) on the surface, which change the surface structure and porosity and can reduce the surface coverage of the low work function BaO layer. One of the major drawbacks of using BaO dispenser cathodes in electric propulsion applications is the extremely high feed gas purity specified to avoid these poisoning and tungsten-material transport issues, which has resulted in a special "propulsion-grade" xenon with 99.9995% purity to be specified by some users of these cathodes for flight.

Another electron emitter material, lanthanum hexaboride [13], is a crystalline material made by press sintering $LaB_6$ powder into rods or plates and then machining the material to the desired shape. Polycrystalline $LaB_6$ cathodes have a work function of about 2.67 eV, depending on the surface stoichiometry, and will emit over 10 $A/cm^2$ at a temperature of 1650˚C, as shown in Fig. 6-7. Since the bulk material is emitting, there is no chemistry directly involved in establishing the low work function surface, and $LaB_6$ cathodes are insensitive to impurities and air exposures that can destroy a BaO dispenser cathode [18]. An $LaB_6$ cathode can withstand gas-feed impurity levels two orders of magnitude higher than dispenser cathodes at the same emission current density. In addition, the cathode life is determined primarily by the low evaporation rate of the $LaB_6$ material at typical operating temperatures. The higher operating temperature of bulk $LaB_6$ and the need to support and make electrical contact with $LaB_6$ with materials that inhibit boron diffusion at the operating temperatures require some careful engineering of the cathode structure. However, $LaB_6$ cathodes are commonly used in Russian Hall thrusters in communications satellite applications [19].

Lanthanum hexaboride was first developed as an electron emitter by Lafferty [13] in the 1950s. The thermionic emission of lanthanum–boron compounds for various surface stoichiometries was extensively studied by several authors [14,15,19]. The first flight of Russian SPT Hall thrusters [20] in 1971, and all subsequent flights, utilized lanthanum hexaboride cathodes. The first reported use of $LaB_6$ in the US in a hollow cathode was by Goebel, et al. [21] in 1978, and the development of a high-current $LaB_6$ cathode for plasma sources that

dealt with supporting and making electrical contact with the material was described by Goebel, et al. [22] in 1985. The lanthanum–boron system can consist of combinations of stable $LaB_4$, $LaB_6$, and $LaB_9$ compounds, with the surface color determined [23] by the dominate compound. The evolution of $LaB_4$ to $LaB_9$ compounds is caused either by preferential sputtering of the boron or lanthanum atoms at the surface by energetic ion bombardment [14] or by preferential chemical reactions with the surface atoms [23]. However, a lanthanum–boride compound, when heated in excess of 1000°C in a reasonable vacuum, will evaporate its component atoms at rates that produce a stable $LaB_{6.0}$ surface.

Dispenser cathodes and $LaB_6$ cathodes offer long lifetimes in thruster applications because the evaporation rate is significantly lower than for refractory metals. Figure 6-8 shows the evaporation rate as a function of the emission current density for a Type S 4:1:1 dispenser cathode [17], $LaB_6$ [24], and tungsten [8] (for comparison). The dispenser cathode and $LaB_6$ cathode evaporation rates are more than one order of magnitude lower when compared with tungsten at the same emission current density. Excessive evaporation of barium and reduced surface coverage usually limit the current density of dispenser cathodes to less than about 20 $A/cm^2$ in continuous operation. In spite of operating at a significantly higher temperature than the barium cathode, the $LaB_6$ has a lower evaporation rate until the emission current exceeds about 15 $A/cm^2$ and can provide longer life. The life of these cathodes is discussed in more detail in Section 6.8.
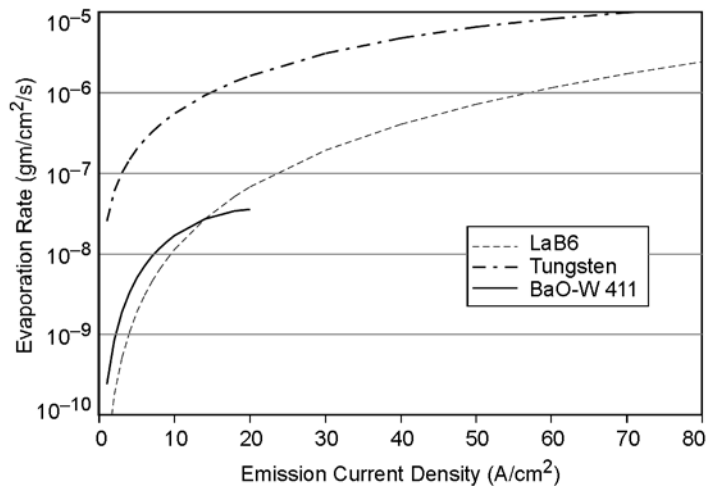


**Fig. 6-8. Evaporation rate of Type-S 4:1:1-dispenser cathodes, $LaB_6$ and tungsten.**

## 6.4  Insert Region Plasma

The insert region of the hollow cathode, as was illustrated in Fig. 6-4, usually has a cylindrical geometry with electron emission from the interior surface of a thermionic insert material. A plasma discharge is established inside the insert region, and electrons emitted from the insert surface are accelerated through the cathode sheath that forms between the insert surface and the plasma. The insert plasma must be capable of accepting the emitted electron current from the sheath and must provide heating of the insert for the cathode to operate properly. The maximum electron current density into the insert plasma is then determined by either space-charge limitations in the plasma at the sheath edge or by characteristics of the surface (work function and temperature) that limit the thermionic emission. As shown by the double sheath analysis in Chapter 3, ions flowing back from the plasma through the sheath to the cathode surface neutralize the electron space charge and increase the extracted electron current density from the insert surface. The electrons accelerated through the sheath quickly give up their energy to the dense collisional plasma inside the insert. Electrons in the tail of the Maxwellian distribution in this plasma have sufficient energy to ionize some portion of the thruster propellant injected through the cathode, which is only a small fraction of the total propellant injected into the thruster. Plasma electrons incident on the downstream end of the cathode tube flow through the orifice and into the main discharge chamber.

The barium evaporated from dispenser cathode inserts is easily ionized in plasmas with this electron temperature because its ionization potential is only 5.2 eV. A calculation of the ionization mean free path in NASA Solar Electric Propulsion Technology Applications Readiness (NSTAR)-sized hollow cathodes [25] predicts about $4 \times 10^{-5}$ m, which is much smaller than the interior dimensions of the cathode. The ionized barium then migrates upstream because the potential gradient in the hollow cathode that pulls electrons out of the cathode plasma also accelerates barium ions in the opposite direction (upstream). This means that the barium in the insert does not leave the cathode during discharge operation, but tends to travel upstream in the plasma and is deposited in the cooler sections of the hollow cathode.

The pressure inside the hollow cathode is set primarily by the gas flow rate through the cathode and the orifice size and must be sufficiently high to produce a collisional plasma. This condition is required to slow ions backstreaming from the orifice region and from the peak plasma potential on axis (primarily by charge exchange) to avoid sputtering of the insert surface by high-energy ion bombardment. While this condition may not necessarily be satisfied everywhere inside a Type C cathode (with no orifice), at least some fraction of the insert is protected by the collisional processes for proper cathode

operation and life. The collisional plasma will also tend to have a low electron temperature, which reduces the sheath voltages and further protects the low work function insert surface from damage or modification by the plasma.

It is possible to describe [26] the insert plasma using simple particle and energy balance models and plasma diffusion models because the plasma transport inside the hollow cathode is dominated by collisions. In Chapter 3, the solution to the radial diffusion equation for ions in collisionally dominated plasmas in cylindrical geometry resulted in an eigenvalue equation with a unique dependence on the electron temperature:

$$\left(\frac{R}{\lambda_{01}}\right)^2 n_o \sigma_i (T_e) \sqrt{\frac{8kT_e}{\pi m}} - D = 0 , \tag{6.4-1}$$

where $R$ is the internal radius of the insert, $\lambda_{01}$ is the first zero of the zero-order Bessel function, $n_o$ is the neutral density, $\sigma_i$ is the ionization cross section averaged over a Maxwellian electron temperature, and $D$ is the diffusion coefficient. This means that the electron temperature is constrained to produce sufficient ions to offset the diffusion losses to the wall.

The diffusion in the radial direction in the insert region is ambipolar, and the ion mobility is limited by resonant charge exchange (CEX) with the xenon neutral atoms. The average collisions frequency for the ions is then

$$v_i = \sigma_{\text{CEX}} \, n_o \, v_{\text{scat}} , \tag{6.4-2}$$

where the effective velocity for scattering of the ions in the insert region is approximated by the ion thermal speed:

$$v_{\text{scat}} = \sqrt{\frac{kT_i}{M}} . \tag{6.4-3}$$

Since the electron mobility is much higher than the ion mobility, the ambipolar diffusion coefficient $D_a$ from Eq. (3.6-58) for this case is then

$$D_a = D_i \left(1 + \frac{T_e}{T_i}\right) = \frac{e}{M} \frac{\left(T_{iV} + T_{eV}\right)}{\sigma_{\text{CEX}} \, n_o \, v_{\text{scat}}} , \tag{6.4-4}$$

where the ion and electron temperatures are shown in eV. As an example, take two hollow cathodes operating in xenon with different inside diameters of the insert. The neutral density inside the hollow cathode is described by Eq. (2.7-2) for a given pressure, determined by the gas flow and the orifice size. A simple analytical technique to estimate the neutral pressure in the insert region is given

in Appendix B. Typical pressures inside discharge hollow cathodes usually range from 1 to 15 torr, although higher pressures are often used in neutralizer cathodes. Figure 6-9 shows the electron temperature versus internal pressure found from Eq. (6.4-1) for two insert diameters, assuming a charge exchange cross section of $10^{-18}$ m$^2$ [27] for low temperature xenon ions and neutrals inside the hollow cathode and a neutral gas temperature of 2500 K. The smaller NSTAR insert diameter requires a higher electron temperature to offset the higher diffusion losses to the closer wall at a given pressure. During operation at the high power TH15 throttle point at 13.1 A and 3.7 sccm, the internal pressure is measured to be about 7.5 torr, and the predicted electron temperature is then about 1.36 eV. This agrees well with probe data taken in the insert region [28] in this mode. The NEXIS cathode nominal discharge conditions of 25 A and 5.5 sccm produce an internal pressure of 1.8 torr, which results in a predicted electron temperature of about 1.4 eV that is also in good agreement with the measurements [28].

The radially averaged ion density in the hollow cathode is related to the ion density on the cathode centerline by

$$\bar{n} = \frac{\int_0^R n(0) J_o\left(\frac{\lambda_{01}}{R} r\right) 2\pi r \, dr}{\pi R^2} = n(0)\left[\frac{2 J_1(\lambda_{01})}{\lambda_{01}}\right]. \qquad (6.4\text{-}5)$$

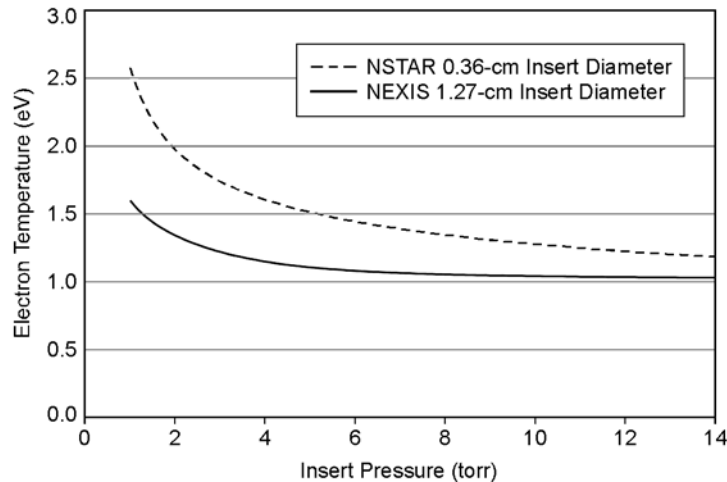The ion flux going radially to the wall is



Fig. 6-9. Electron temperature in the insert region as a function of internal pressure for two cathode insert inner diameters.

$$J_i = \bar{n}v_r = -D_a \frac{\partial n}{\partial r} = n(0) D_a \frac{\lambda_{01}}{R} J_1(\lambda_{01}) = \bar{n}D_a \frac{(\lambda_{01})^2}{2R}. \qquad (6.4\text{-}6)$$

Using the ambipolar diffusion coefficient from Eq. (6.4-4), the effective radial drift velocity at the wall is then

$$v_r = \frac{(2.4)^2}{2R\sigma_{\text{CEX}} \, n_o \, v_{\text{scat}}} \frac{e}{M} \left(T_{iV} + T_{eV}\right). \qquad (6.4\text{-}7)$$

In the example above, the larger-diameter insert produces an electron temperature of about 1.4 eV at 1.8-torr internal xenon pressure. The effective ion velocity found near the wall outside the sheath is only 3.1 m/s due to the ion-neutral CEX collisions, which slows the ion velocity to significantly less than the 500-m/s ion thermal velocity and 1200-m/s xenon ion acoustic velocity. Since the pre-sheath potential that accelerates the ions to the Bohm velocity prior to entering the sheath extends only the order of the collision mean free path into the plasma, ions diffusing to the plasma edge are accelerated very close to the sheath to the Bohm velocity due to the high collisionality in the insert plasma.

The density of the insert plasma can be estimated by a simple 0-dimensional (0-D) particle and energy balance model. These types of models assume a fairly uniform plasma in the insert region and so provide density estimates within factors of the order of two. In the insert plasma, heating of the plasma is balanced by the energy loss:

$$I_t\phi_s + RI_e^2 = I_iU^+ + \frac{5}{2}T_{eV}I_e + \left(2T_{eV} + \phi_s\right)I_r e^{-\phi_s/T_{eV}}, \qquad (6.4\text{-}8)$$

where $I_t$ is the thermionic electron current, $\phi_s$ is the cathode sheath voltage, $R$ is the plasma resistance, $I_e$ is the hollow cathode discharge current, $I_i$ is the total ion current generated in the insert region, $U^+$ is the ionization potential, $T_{eV}$ is the electron temperature (in volts), and $I_r$ is the random electron flux at the sheath edge. In this case, excitation and radiation losses seen in the discharge chamber energy balance equations are ignored because the high density plasma inside the hollow cathode is optically "thick" and the radiated energy is reabsorbed by the plasma. The resistance, $R$, is the resistivity times the average conduction length, $\ell$, divided by the cross-sectional area of the plasma:

$$R = \eta \frac{\ell}{\pi r^2}. \qquad (6.4\text{-}9)$$

The resistivity of the plasma is given from Eq. (3.6-21) by

$$\eta = \frac{1}{\varepsilon_o \, \tau_e \, \omega_p^2}, \qquad (6.4\text{-}10)$$

where the collision time, $\tau_e$, for electrons, accounting for both electron-ion and electron-neutral collisions, is given by

$$\tau_e = \frac{1}{\upsilon_{ei} + \upsilon_{en}}, \qquad (6.4\text{-}11)$$

where $\upsilon_{ei}$ is the electron-ion collision frequency given in Eq. (3.6-14) and $\upsilon_{en}$ is the electron-neutral collision frequency given in Eq. (3.6-12) from [29].

At the insert, power balance gives

$$H(T) + I_t \phi_{wf} = I_i \left( U^+ + \phi_s + \frac{T_{eV}}{2} - \phi_{wf} \right) + \left( 2T_{eV} + \phi_{wf} \right) I_r e^{-\phi_s / T_{eV}}, \quad (6.4\text{-}12)$$

where $H(T)$ is the total heat lost by the insert due to radiation and conduction and $\phi_{wf}$ is the cathode work function. Particle conservation in the discharge dictates that

$$I_e = I_t + I_i - I_r e^{-\phi_s / T_{eV}}. \qquad (6.4\text{-}13)$$

The random electron flux within a collision length of the sheath edge is given by

$$I_r = \frac{1}{4} \left( \frac{8kT_e}{\pi m} \right)^{1/2} n_e \, e \, A, \qquad (6.4\text{-}14)$$

where the plasma density, $n_e$, is evaluated at the sheath edge. The ion current is given by the Bohm current in Eq. (3.7-29), where the ion density is again evaluated within one collision length of the sheath edge.

Equations (6.4-8), (6.4-12), (6.4-13), and (6.4-14) can be combined to eliminate the ion current term, which gives

$$\frac{RI_e^2 + I_e \left( \phi_s + \frac{5}{2} T_{eV} \right)}{H(T) + I_e \phi_{wf}} = \frac{U^+ + \phi_s + 2T_{eV} \left( \dfrac{2M}{\pi m} \right)^{1/2} e^{-\phi_s / T_{eV}}}{U^+ + \phi_s + \dfrac{T_{eV}}{2} + 2T_{eV} \left( \dfrac{2M}{\pi m} \right)^{1/2} e^{-\phi_s / T_{eV}}}. \quad (6.4\text{-}15)$$

Since the electron temperature is given by the solution to Eq. (6.4-1) in the insert region (as shown above), Eq. (6.4-15) can be solved for the cathode sheath voltage as a function of the discharge current if the radiation and conduction heat losses are known. The insert heat losses are found from thermal models of the cathode, which will be discussed in Section 6.6. Equation (6.4-15) can be greatly simplified by realizing that in most cases $T_{eV} / 2 << (U^+ + \phi_s)$, and the right-hand side is essentially equal to one. Equation (6.4-15) then reduces to a simple power balance equation, and the cathode sheath voltage is

$$\phi_s = \frac{H(T)}{I_e} + \frac{5}{2} T_{eV} + \phi_{wf} - I_e R. \tag{6.4-16}$$

Figure 6-10 shows the calculated sheath voltage from Eq. (6.4-16) for the NSTAR cathode at a fixed 3.7-sccm xenon flow rate as a function of the discharge current for four values of the combined radiated and conducted power loss. From Fig. 6-9, the electron temperature is taken to be 1.36 eV for the 7.8 torr measured at 13 A of discharge current and this flow. A thermal model of this cathode [30] indicates that the insert heat loss is about 13 W at 13 A of discharge current, resulting in a sheath voltage from the figure of only about 3.6 V. In this case, a significant fraction of the 1.36 eV electron-temperature plasma electrons can overcome the sheath voltage and be collected on the insert to provide heating. The balance of the power required to heat the insert in the NSTAR cathode comes from orifice plate heating [30], which will be discussed in the next section.
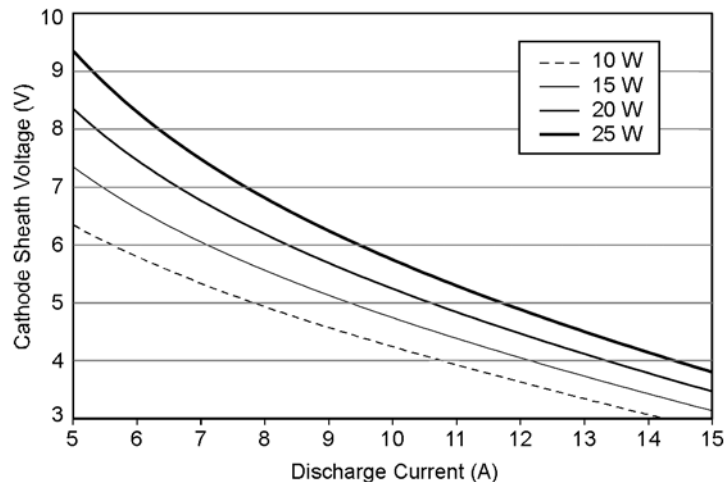


**Fig. 6-10. Insert sheath voltage versus discharge current for the NSTAR cathode for four values of the radiated and conducted heat loss.**

In low-pressure Type B and C cathodes, the sheath potentials are much greater than the 3.6 V calculated for the NSTAR discharge cathode. For example, in Fig. 6-9, the NSTAR solution for the electron temperature at the far right of the graph is in excess of 7 torr, while NEXIS and other large orifice cathodes are closer to the left side of the graph, between 1 and 2 torr. The sheath potential found by solving Eq. (6.4-16) for the NEXIS electron temperature is over 7 V, and so relatively few plasma electrons return to the emitter and do little heating. Most of the insert heating in lower pressure (on the order of 1 to 2 torr), lower internal plasma density cathodes is from ion bombardment of the insert surface due to the higher sheath voltage.

The insert plasma density can now be found from Eq. (6.4-8). The ion current term is given by

$$I_i = n_o \bar{n}_e e \langle \sigma_i v_e \rangle V , \qquad (6.4\text{-}17)$$

where $n_o$ is the neutral density, $< \sigma_i v_e >$ is the ionization reaction rate coefficient, $V$ is the volume, and $\bar{n}_e$ is the average plasma density over the insert volume. Remembering that the plasma density in the random electron flux equation is evaluated at the plasma edge, Eq. (6.4-8) can be solved using the above equations to produce an expression for the average plasma density:

$$\bar{n}_e = \frac{RI_e^2 - \left(\dfrac{5}{2}T_{eV} - \phi_s\right)I_e}{\left[ f_n\, T_e \left(\dfrac{kT_e}{2\pi m}\right)^{1/2} eA e^{-\phi_s/T_{eV}} + n_o e \langle \sigma v_e \rangle V \left(U^+ + \phi_s\right) \right]} , \quad (6.4\text{-}18)$$

where $f_n$ is the edge-to-average plasma density ratio. Since the electrons in the insert plasma are Maxwellian, the value of $f_n$ can be estimated from the potential difference between the center and the edge:

$$f_n = \frac{n_e}{\bar{n}_e} \approx e^{-\left(\phi_{\text{axis}} - \phi_s\right)/T_{eV}} , \qquad (6.4\text{-}19)$$

where the potential on axis $\phi_{\text{axis}}$ must come from measurements or two-dimensional (2-D) codes. The plasma density calculated from Eq. (6.4-18) for the NSTAR discharge cathode at a constant xenon gas flow of 3.7 sccm, using the electron temperature from the radial diffusion model (Fig. 6-9), the sheath potential from the power balance model (Fig. 6-10), and a measured on-axis plasma potential of about 8.5 V [6], is shown in Fig. 6-11. Good agreement with the plasma density measurements made by a miniature scanning probe in this cathode [28] is obtained, and a nearly linear dependence on discharge
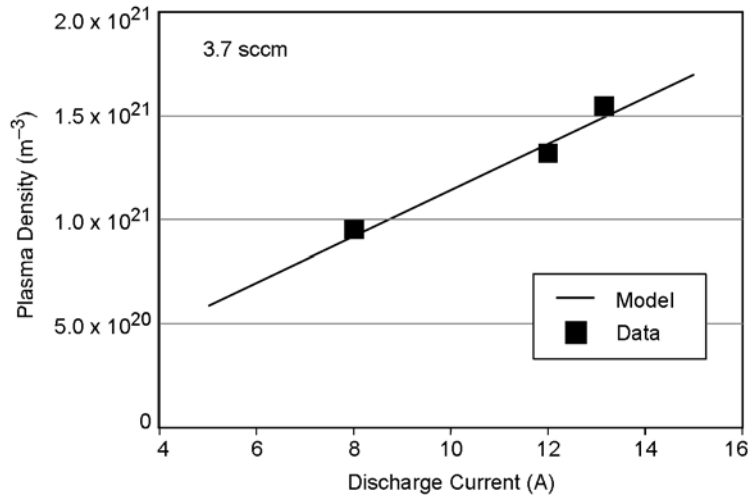
**Fig. 6-11. Peak plasma density calculation for the NSTAR cathode operating at a constant gas flow of 3.7 sccm.**

current is predicted by the model and shown experimentally. While the simple 0-D cathode model requires insert heat loss from a cathode thermal model and on-axis potentials from probe measurements or 2-D code runs, it provides reasonable agreement with the data and illustrates the dependence of the insert plasma density and temperature on the geometry and the plasma conditions inside the cathode.

The 0-D model also illuminates the heating mechanism in the hollow cathode. The ion heating to the insert is found in Eq. (6.4-12):

$$\text{Power}_{\text{ions}} = I_i \left( U^+ + \phi_s + \frac{T_{eV}}{2} - \phi_{wf} \right), \qquad (6.4\text{-}20)$$

where the ion current is given by the Bohm current at the sheath edge. Using the above parameters for the Type B NSTAR discharge cathode shown in Fig. 6-5 at the full-power TH15 operating point of 13 A and 3.7 sccm ($U^+ = 12.1$ eV, $\phi_s = 3.6$ eV, $T_e = 1.36$ eV, $\phi_{wt} = 2.06$ V, $\phi_{\text{axis}} = 8.5$ V, and $n_i \approx 1.5 \times 10^{21}$ m$^{-3}$), the ion heating power from Eq. (6.4-20) is only 4.7 W. The electron heating of the insert is also found in Eq. (6.4-12):

$$\text{Power}_{\text{electrons}} = \left( 2T_{eV} + \phi_{wf} \right) I_r e^{-\phi_s / T_{eV}}, \qquad (6.4\text{-}21)$$

where the random electron flux is again evaluated at the sheath edge. For the same parameters for the Type B NSTAR cathode given in the paragraph above, the electron heating of the insert is found to be about 45 W. This Type B

cathode is, therefore, heated predominately by electron heating of the insert, with a comparable amount coming from orifice heating (shown in the next section). Similar analysis of Type B cathodes with larger orifices or lower flow rates, and also most Type C cathodes, indicates that ion heating will become the dominant heating mechanism due to the higher electron temperature and larger sheath potential drop at the insert.

It is important to recognize that, as the pressure in the hollow cathode is increased, much of plasma heating comes from resistive heating of the current flowing through the partially ionized plasma. The higher the neutral gas background pressure, the greater the contribution of resistive heating. In cathodes with larger orifices that produce lower internal pressures, most of the heating of the insert plasma comes from the emitted electrons being accelerated across the cathode sheath potential. In lower pressure cathodes, the sheath potential is higher and the plasma resistivity is lower, resulting in less joule heating of the plasma but more ion bombardment heating of the insert surface. This is illustrated in Fig. 6-12, which shows the sheath potential and the ion and electron currents impacting the cathode as a function of the resistive joule heating of the plasma.

The behavior shown in Fig. 6-12 can be understood by rearranging the equations in the power balance model above. Using Eqs. (6.4-13) and (6.4-14) in the power balance equation [Eq. (6.4-8)] and solving for the sheath potential gives

$$\phi_s = \frac{-RI_e^2 + I_i U^+ + \frac{5}{2} T_{eV} I_e + \left(2 T_{eV} + \phi_s\right) I_i \sqrt{\dfrac{2 m_i}{\pi m_e}} \exp(-\phi_s / T_{eV})}{\left(I_e - I_i \left(1 - \sqrt{\dfrac{2 m_i}{\pi m_e}} \exp(-\phi_s / T_{eV})\right)\right)} . \quad (6.4\text{-}22)$$

The decrease in the sheath potential observed in Fig 6-12 as the joule heating ($RI_e^2$) becomes more significant follows directly from Eq. (6.4-22), because the joule heating term enters with a negative sign. Equation (6.4-13) also shows that a decrease in the sheath potential allows for more of the electron flux to return to the emitter. Finally, if the heat loss, $H(T)$, is fixed, Eq. (6.4-12) shows that the increased electron return flux (second term on the right-hand side) must be balanced by a reduced ion flux (first term on the right-hand side). This illustrates how the design and operating conditions of the hollow cathode (sizes, flow, and discharge current) determine which terms dominate in the cathode self-heating.
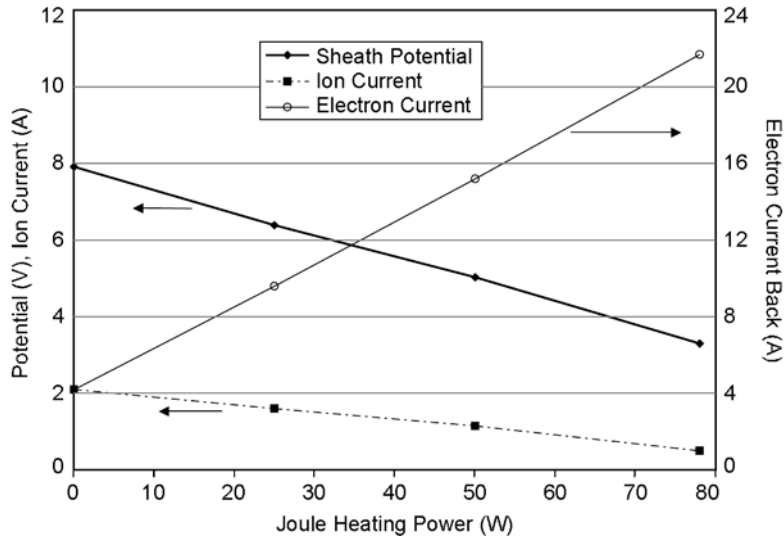
**Fig. 6-12. Sheath potential and currents to the insert as a function of the resistive joule heating in the insert plasma.**

It is also possible to estimate the axial extent of the plasma in the insert region for Type A and some Type B cathodes with small orifices that again produce diffusion-dominated plasmas. This is useful in understanding the plasma "attachment" or "contact length" with the insert, which impacts where the electron emission can take place. As was shown in Chapter 3, the solution to the 2-D diffusion equation in cylindrical geometry is the product of a zero-order Bessel function radially times an exponential term in the axial direction:

$$n(r,z) = n(0) J_o\left(\sqrt{C^2 + \alpha^2}\; r\right) e^{-\alpha z}, \qquad (6.4\text{-}23)$$

where $\alpha$ is one over the $e$-folding distance of the plasma density from the reference location on axis at (0,0). This length can be found by considering the ion generation inside the insert. The ion current to the insert surface is the ion generation rate integrated over the volume inside the insert:

$$I_i = 2\pi \int_0^R \int_0^L n_o n e \sigma_i v_e \, r \, dr \, dz . \qquad (6.4\text{-}24)$$

Taking the axial integral in Eq. (6.4-24) to be approximately the $e$-folding distance ( $L = 1/\alpha$ ), Eq. (6.4-24) is simply

$$I_i = \frac{\pi R^2}{\alpha} n_o \bar{n} e \langle \sigma_i v_e \rangle . \qquad (6.4\text{-}25)$$

The average plasma density is found from Eq. (6.4-5):

$$\bar{n} = n(0,0)\left[\frac{2J_1(\lambda_{01})}{\lambda_{01}}\right] = n(0,0)\left[\frac{(2)(0.5191)}{2.4048}\right] = 0.43n(0,0). \quad (6.4\text{-}26)$$

Using Eq. (6.4-26) in Eq. (6.4-25) and solving for the value of $\alpha$ gives

$$\alpha = \frac{0.43\pi R^2}{I_i} n_o n(0,0)e\langle\sigma_i v_e\rangle. \quad (6.4\text{-}27)$$

For example, the axial plasma density profile from the scanning probe inside the NSTAR hollow cathode [31] operating at 15 A and 3.7 sccm is shown in Fig. 6-13. Taking the peak plasma density from the figure of $n(0,0) = 1.6 \times 10^{21}$ m$^{-3}$ as the reference density at position (0,0) and using the neutral density, calculated inside the insert from Eq. (2.7-2), of $2.5 \times 10^{22}$ m$^{-3}$, Eq. (6.4-27) gives a value of $\alpha = 6.0$ if the ion current to the insert is 0.5 A. The fit to the exponential decrease in the plasma density upstream of the orifice shown in Fig. 6-13 gives $\alpha = 6.1$. The assumed value of 0.5 A for the ion current actually results from a two-dimensional model of the insert plasma [5], which will be discussed below. This simple diffusion model shows an exponential behavior in the axial plasma density profile, predicted from Eq. (6.4-23), which is consistent with the near-exponential profiles measured in the NSTAR cathode sufficiently far away from the orifice region.

A closer examination of Eq. (6.4-27) shows that the terms on the right-hand side represent the ionization rate per unit volume. If the geometry of the
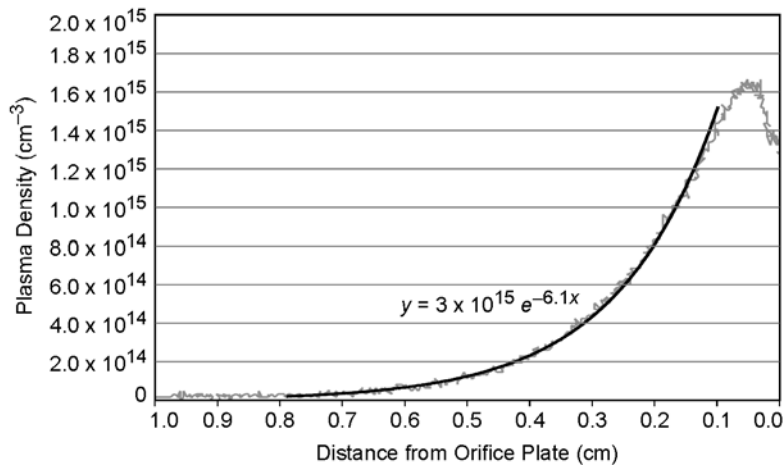


Fig. 6-13. Plasma density measured on axis in the insert region for an NSTAR cathode operating at TH15.

cathode is fixed, then the number of ions flowing to the insert ($I_i$ in the denominator) is proportional to this ionization rate per unit volume. Therefore, the value of alpha will be constant for varying operating conditions of a given size of cathode. This behavior is illustrated in Fig. 6-14, where the density profile for an NSTAR-sized cathode with two different orifice sizes operating at the same discharge current and gas flow is shown. For the larger orifice cathode, the internal pressure at the constant gas flow is lower, and the penetration of the 2-D effects associated with the downstream boundary condition and the electron current funneling into the orifice extends deeper into the insert region. However, once the collisionality establishes a diffusion-limited plasma flow to the insert upstream of the orifice, then Eq. (6.4-23) is again valid and the value of alpha in the cathode is seen to be essentially constant.

It should be noted that the *e*-folding distance for the plasma density measured inside the NSTAR cathode in Fig. 6-13 is $1/\alpha = 1.7$ mm. Therefore, the plasma in the small orifice case is only in significant contact with the insert for a few *e*-foldings, which is less than 1 cm. This rapid plasma density decrease away from the orifice is the result of the very high pressure in the NSTAR cathode [5,6,] and also occurs in most neutralizer cathodes. For high-pressure cathodes like this, utilizing inserts significantly longer than 1 to 1.5 cm in length is not very useful because there is little plasma left beyond this distance to accept the thermionic emission from the insert.
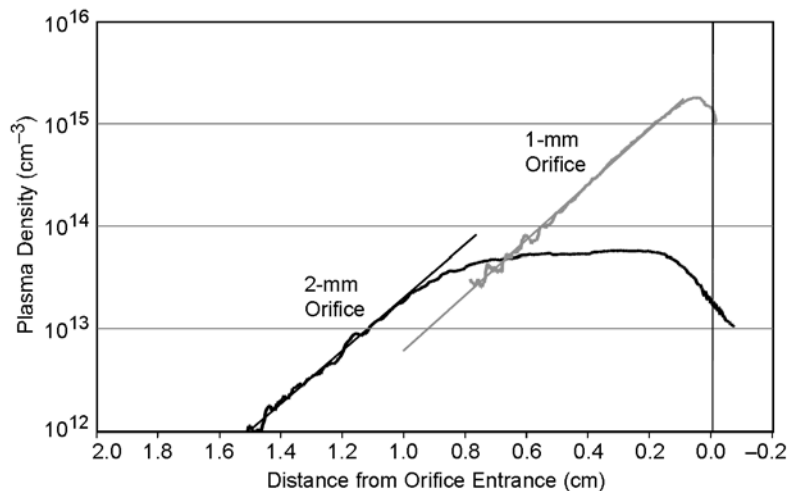


**Fig. 6-14. Plasma density measured on axis in the insert region for an NSTAR-sized cathode operating at TH15 with two different orifice sizes.**

While the 0-D and one-dimensional (1-D) models described above can provide insight into the operation of hollow cathodes, to self-consistently calculate the plasma density in the insert region, including the effects near the cathode orifice, requires a two-dimensional model [32]. The insert plasma energy balance in this model can be found from the electron and ion energy equations. The conservation of energy equations was described in Section 3.5.3 of Chapter 3. The steady-state electron energy equation can be written

$$0 = -\nabla \cdot \left( -\frac{5}{2} \mathbf{J}_e \frac{kT_e}{e} - \kappa \frac{\nabla kT_e}{e} \right) + \eta J_e^2 - \mathbf{J}_e \cdot \frac{\nabla nkT_e}{ne} - \dot{n} e U^+ , \qquad (6.4\text{-}28)$$

where $\mathbf{J}_e$ is the electron current density in the plasma, $\kappa$ is the electron thermal conductivity given by Eq. (3.5-29), $\eta$ is the plasma resistivity given by Eq. (3.6-21), and $U^+$ is the ionization potential of the neutral gas. The steady-state ion energy equation is

$$0 = -\nabla \cdot \left( -\frac{5}{2} \mathbf{J}_i \frac{kT_i}{e} - \kappa_n \frac{\nabla kT_i}{e} \right) + \mathbf{v}_i \cdot \nabla \left( nkT_i \right) + nM \nu_{in} v_i^2 + Q_T , \qquad (6.4\text{-}29)$$

where $\mathbf{J}_i$ is the ion current density, $\kappa_n$ is the thermal conductivity for neutrals, and it is assumed that the ions and neutrals are in thermal equilibrium ($T_n = T_i$) in the collisional insert plasma.

The energy balance equations are used to close the system of equations describing the plasma in the insert region. These equations also are used to describe the self-heating mechanism characteristic of hollow cathodes due to the particle flux and energy hitting the cathode walls. This effect will be discussed in Sections 6.5 and 6.6 with respect to the cathode thermal models.

Writing the steady-state momentum equations from Eq. (3.5-5) for the ions and electrons,

$$0 = en\mathbf{E} - \nabla \cdot \mathbf{p}_i - Mn \left[ \nu_{ie} \left( \mathbf{v}_i - \mathbf{v}_e \right) + \nu_{in} \left( \mathbf{v}_i - \mathbf{v}_n \right) \right], \qquad (6.4\text{-}30)$$

$$0 = -en\mathbf{E} - \nabla \cdot \mathbf{p}_e - mn \left[ \nu_{ei} \left( \mathbf{v}_e - \mathbf{v}_i \right) + \nu_{en} \left( \mathbf{v}_e - \mathbf{v}_n \right) \right]. \qquad (6.4\text{-}31)$$

Adding these two equations, assuming that the neutrals move slowly compared to the charged particles, and writing the result in terms of the ion and electron fluxes gives

$$\mathbf{J}_i = \frac{m}{M} \frac{\nu_{en}}{\nu_{in} \left( 1 + \nu \right)} \mathbf{J}_e - \frac{\nabla \left( nkT_i + nkT_e \right)}{M \nu_{in} \left( 1 + \nu \right)} , \qquad (6.4\text{-}32)$$

where $v = v_{ie} / v_{in}$.

Combining Eq. (6.4-32), which is known as the generalized Ohm's law, with the sum of the ion and electron continuity equations,

$$\nabla \cdot \left( \mathbf{J}_e + \mathbf{J}_i \right) = 0 , \qquad (6.4\text{-}33)$$

gives the particle balance equation,

$$\nabla \cdot \left( \frac{\nabla \phi}{\eta} \right) = \nabla \cdot \left[ \frac{\nabla \left( nkT_e \right)}{\eta ne} + \mathbf{J}_i \left( 1 - \frac{v_{ei}}{v_{en} + v_{ei}} \right) \right] , \qquad (6.4\text{-}34)$$

where the electric field is $\mathbf{E} = -\nabla \phi$. The total resistivity in the plasma in Eq. (6.4-34) is given by combining Eqs. (6.4-9) and (6.4-10):

$$\eta = \frac{m\left( v_{en} + v_{ei} \right)}{ne^2} . \qquad (6.4\text{-}35)$$

These equations have been used in a full 2-D code [5] to find the plasma density, temperature, and potential in the insert region for the NSTAR discharge operating conditions of 12 A and 4.25 sccm. Utilizing thermionic emission from the insert surface, described by Eq. (6.3-4), with temperatures measured by Polk [33], and applying the proper boundary conditions, the plasma density profile along the axis of symmetry is compared with the laboratory measurement in Fig. 6-15. The 12-A net cathode current was found to result from almost 32-A electron emission by the insert countered by 20 A of plasma (thermal) electron current back to the insert and the orifice plate. The particle balance in the insert is shown in Table 6-2, where only about one-half ampere of the net cathode current is due to ionization of the xenon gas. This is consistent with the previous analysis used to obtain the exponential density scale lengths.

The 2-D code adequately describes what is happening in the cathode insert region. For example, the numerical results in Table 6-2 capture the 2-D effects upstream of the cathode orifice, predicting a density profile that is consistent with the data [2] shown in Fig. 6-16. The code's predictions of the electron temperature and plasma potential are also close to the measured values in the emission zone, which extends less than about 0.5 cm upstream of the orifice entrance in the NSTAR cathode. Figure 6-16(a) shows that the plasma density falls radially, as expected, toward the insert wall. The 2-D plasma potential contours for this case are also shown in Fig. 6-16(b). Good agreement with the measurements has been achieved with this model for larger cathodes as well, such as with the 1.5-cm-diameter NEXIS cathode [5].
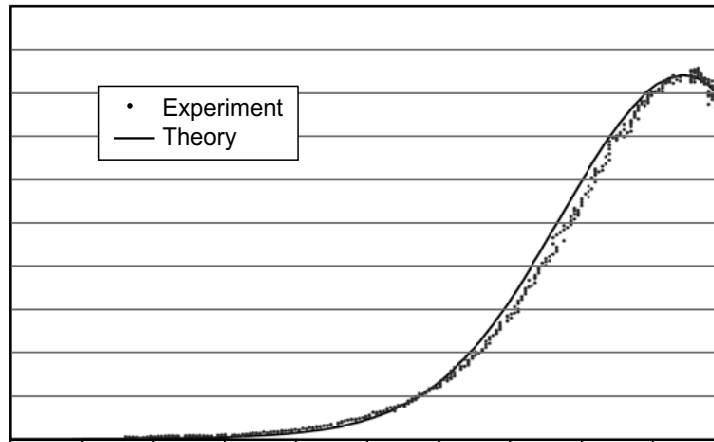
**Fig. 6-15. Comparison of the plasma density measured on axis in the NSTAR-sized cathode operating at 12 A and a 4.25-sccm xenon flow with the 2-D code predictions.**

**Table 6-2. Currents from the 2-D cathode code for the insert plasma of the NSTAR cathode.**

| Source | Current (A) |
|---|---|
| Emitted Electrons | 31.7 |
| Absorbed Electrons | 20.2 |
| Absorbed Ions | 0.5 |
| Net Current | 12.0 |

## 6.5  Orifice Region Plasma

Electrons are extracted from the insert plasma through the orifice into the discharge chamber or ion beam. For cathodes with no orifice, a transition region exists at the end of the insert and cathode tube where the neutral gas density is sufficiently low and the flow becomes collisionless. Orificed cathodes also have a transition region to collisionless neutral flow, which can occur inside the orifice or slightly downstream depending on the orifice size and the gas flow rate. Inside the orifice, the electron current density is the highest in the entire system. In this region, classical electron scattering with the ions and neutral gas produces resistive heating. The hot electrons then ionize a large fraction of the xenon gas, most of which strikes the orifice wall as ions and heats it. The amount of orifice-plasma resistance and orifice-plate heating depends on the geometry, flow rate, and discharge current. Type A cathodes have long, narrow orifices and high pressures, which lead to high resistivity,
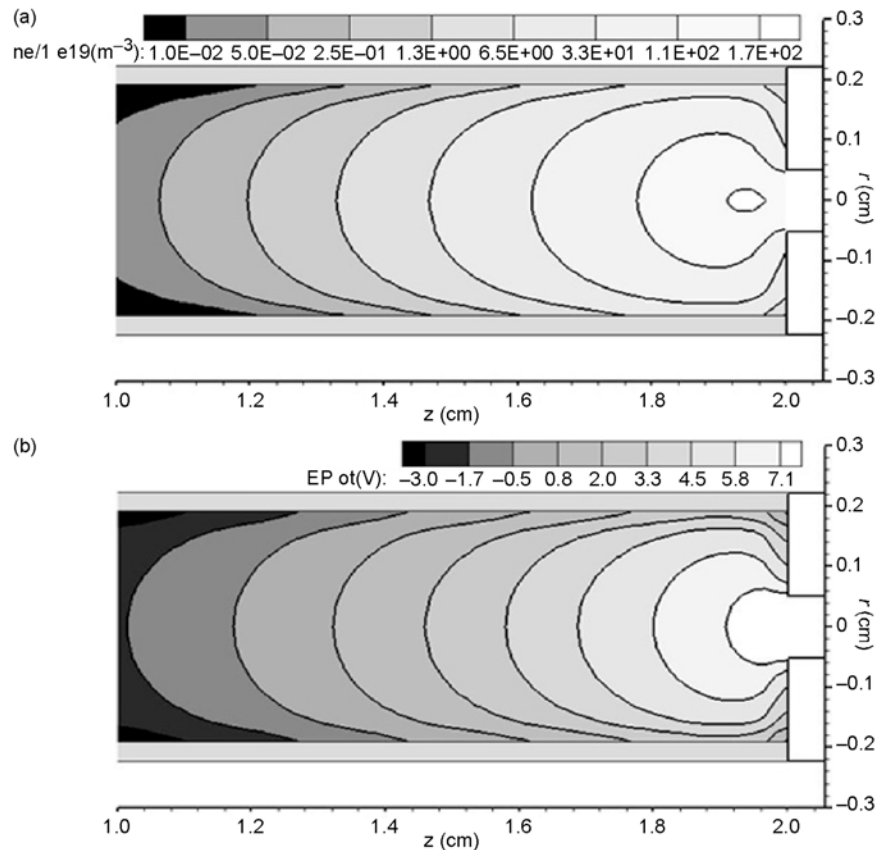
**Fig. 6-16. Density (a) and potential (b) contours plotted for the NSTAR cathode from the OrCa2-D code [5].**

strong ion bombardment of the orifice wall, and significant local heating. Type B cathodes tend to have smaller orifice heating unless the orifice is relatively small and the gas flow high, both because the resistance is usually lower than in Type A cathodes and because a larger fraction of the power deposited in the plasma in this region convects out into the cathode plume. For example, the 1-mm-diameter orifice NSTAR cathode has significant orifice heating, but the 2.5-mm-diameter orifice NEXIS cathode has lower orifice heating even at higher currents.

In Type A and B cathodes, the ion flow in the cylindrical region of the orifice is diffusion limited because of the short collision mean free path for charge exchange with the neutrals. For example, the NSTAR discharge cathode operates at an internal pressure of about 8 torr ( $n_o \approx 5 \times 10^{22}$ m$^{-3}$ ) in the TH15

mode. The mean ion mean free path for resonant CEX collisions for a cross section of $\approx 10^{-18}\,\mathrm{m}^2$ is smaller than even the orifice dimensions:

$$\lambda = \frac{1}{\sigma_{\text{CEX}}\, n_o} \approx 2 \times 10^{-5}\,[\mathrm{m}]. \tag{6.5-1}$$

Thus, diffusion is a good approximation for the ion motion in these hollow cathode orifices.

It is instructive to develop a 0-D model of the cathode orifice plasma to show the dependence of the plasma density, electron temperature, and voltage drop in the orifice region. However, such a model provides only a rough estimate of these parameters because there is a large neutral pressure gradient generated along the orifice, whereas the model uses average parameters. It is assumed for now that the orifice is long compared to its length so that the radial ion diffusion equation applies. The solution to this equation for collisional plasmas in the orifice, described above for the insert region, results in the usual eigenvalue equation dependent on the electron temperature:

$$\left(\frac{r}{\lambda_{01}}\right)^2 n_o\, \sigma_i\left(T_e\right)\sqrt{\frac{8kT_e}{\pi m}} - D = 0\,, \tag{6.5-2}$$

where $r$ is now the internal radius of the orifice, $\lambda_{01}$ is the first zero of the zero-order Bessel function, $n_o$ is the neutral density, $\sigma_i$ is the ionization cross section averaged over a Maxwellian electron temperature, and $D$ is the diffusion coefficient. The electron temperature is again constrained to produce sufficient ions to offset the diffusion losses, as in the insert region analysis. Equation (6.5-2) can be solved for the local electron temperature in the orifice using the terms evaluated in Eqs. (6.4-4) through (6.4-7).

The steady-state electron energy equation [Eq. (6.4-28)] is integrated over the cylindrical orifice, ignoring thermal conduction and radiation losses, to yield an equation for the average plasma density in the orifice. In this case, ohmic heating in the orifice plasma is balanced by convection of the energy deposited in the orifice plasma electrons and ionization losses:

$$I_e^2 R = \frac{5}{2} I_e\left(\frac{kT_e}{e} - \frac{kT_e^{\text{in}}}{e}\right) + n_o\bar{n}_e e\langle\sigma_i v_e\rangle U^+\left(\pi r^2 \ell\right), \tag{6.5-3}$$

where $\ell$ is the length of the orifice. Equation (6.5-3) can be solved for the average plasma density in the orifice:

$$\bar{n}_e = \frac{I_e^2 R - \frac{5}{2} I_e \frac{k}{e}\left(T_e - T_e^{\text{in}}\right)}{n_o e \left\langle \sigma v_e \right\rangle U^+ \pi r^2 \ell} .$$ (6.5-4)

An evaluation of the terms in Eq. (6.5-4) for the orifice region uses the same techniques previously described in Section 6.4 for the insert plasma region. The resistance $R$ is given by Eq. (6.4-9), where the conduction length is now simply the orifice plasma length. The input electron temperature, $T_e^{\text{in}}$, is the electron temperature in the insert plasma that comes from the diffusion model used in Section 6.4 or from experimental measurements.

The detailed measurements of the plasma density and temperature in the orifice of the NSTAR discharge cathode [31] will be used as a first example to compare with the model predictions. The NSTAR discharge cathode has an orifice diameter of 0.1 cm, and the case of the full-power TH15 operating point with 13 A of discharge current at a xenon gas flow rate of 3.7 sccm will be used. The pressure measured inside the insert region for this case is about 7.8 torr [31]. Assuming simple Poiseuille flow (see Appendix B), the pressure in the orifice is estimated to fall to less than 3 torr by the end of the 0.75-mm-long cylindrical section of the orifice. Assuming a gas temperature of about 2000 K in the orifice, the solution for the electron temperature in the diffusion equation [Eq. (6.5-2)] versus pressure in the orifice is shown in Fig. 6-17. The electron temperature predicted by this model varies by less than 1 eV along the orifice length, and the average in the channel is about 2.3 eV. This value is close to the experimentally measured values of 2.2 to 2.3 eV found in this region [28].

Using this electron temperature, the density in the orifice is calculated from Eq. (6.5-2) and plotted in Fig. 6-18 versus the discharge current for the NSTAR cathode. The agreement with the experimental data [31] taken for two discharge currents at the nominal 3.7-sccm cathode flow rate is also very good. The resistance calculated from Eq. (6.4-9) for the cylindrical orifice length is 0.31 ohms, which, at 13 A, produces a voltage drop in the orifice of about 4 V. This is the same magnitude as the voltage change observed in the experimental data, which illustrates that the potential drop in the hollow cathode orifice is resistive due to the very collisional plasma that exists there in these xenon hollow cathodes. Detailed 2-D calculations, described below, indicate that roughly half of the power deposited in this region ($P = 4$ V * 13 A) goes to the orifice wall, and the remainder is convected into the discharge chamber by the plasma.
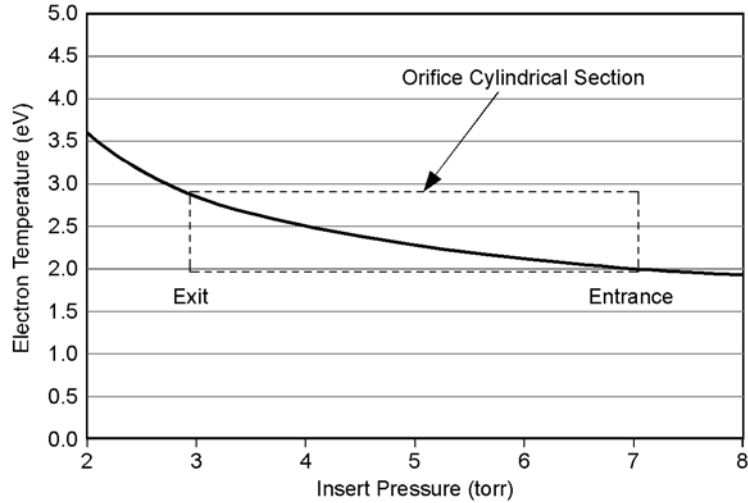
**Fig. 6-17. Orifice electron temperature calculated from the 0-D model through the orifice for the NSTAR discharge cathode at TH15.**
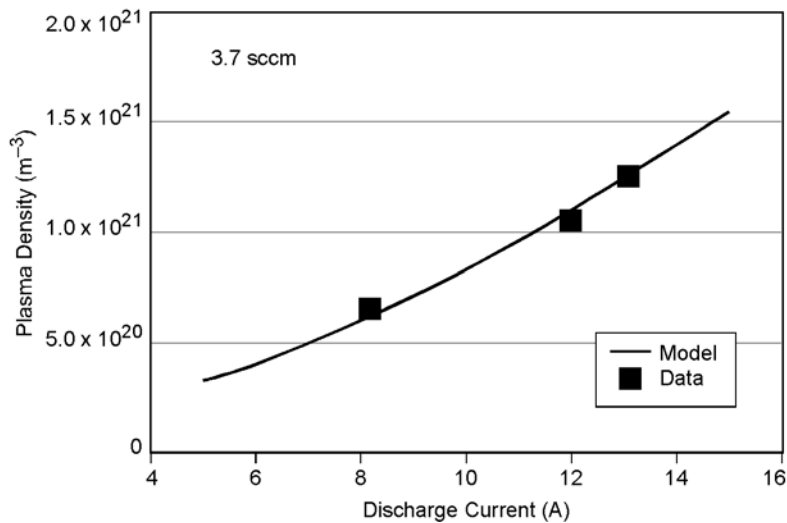


**Fig. 6-18. Orifice plasma density calculated from the 0-D model and measured points for the NSTAR discharge cathode at a 3.7-sccm xenon gas flow.**

Since the 0-D orifice model with just the average parameters has been shown to provide rough estimates of the orifice parameters, it is reasonable to use it to examine Type A cathode orifice heating. Consider the orifice of the NSTAR neutralizer cathode [34], which has an inside diameter of 0.028 cm. The pressure measured inside the neutralizer during operation at 3.2 A, associated

with the full power TH15 case, is 145 torr. Assuming again simple Poiseuille flow (see Appendix B) through the 3:1 aspect ratio orifice channel in this cathode, the pressure is found to fall to less than 20 torr by the end of the 0.75-mm-long cylindrical section of the orifice. Assuming the same gas temperature of about 2000 K in the orifice again, the solution to the radial diffusion, Eq. (6.5-2), predicts the electron temperature to vary by only 0.5 eV along the orifice, with an average value of about 1.4 eV. It is also assumed that a minimal 1-eV electron temperature exists in the insert region for the $T_e^{in}$ in Eq. (6.5-3).

The plasma density in the orifice is plotted in Fig. 6-19 versus the discharge current. At 3.2 A, corresponding to the neutralizer cathode producing the beam current of 1.76 A plus the keeper current of 1.5 A, the predicted plasma density is about $6 \times 10^{22}$ m$^{-3}$. The resistance calculated from Eq. (6.4-9) for the cylindrical orifice section is 3.5 ohms, which, at 3.2 A, produces a resistive voltage drop in the orifice of about 11 V. The power deposited in the plasma ($P = 11$ V $* 3.2$ A $= 35$ W) in this case goes primarily to the orifice wall because the convection power loss is low due to the large geometrical aspect ratio of Type A orifices and the low electron temperature. This demonstrates the resistive orifice heating power characteristically found in Type A cathodes.

While 0-D models are useful to illustrate the strong resistive effects in the orifices of all Type A and some Type B cathodes, the use of average pressures and temperatures reduces the accuracy of these models. However, it is possible to construct a 1-D model for the cathode orifice [35] to address this issue. The
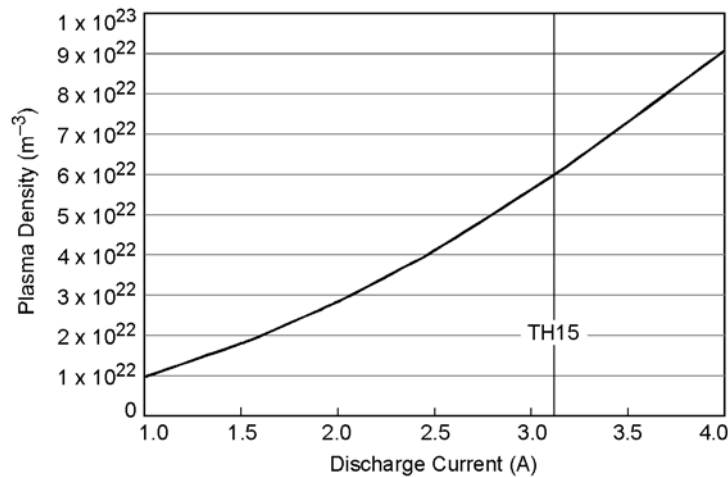


Fig. 6-19. Orifice plasma density calculated from the 0-D model for the NSTAR neutralizer cathode at TH15.

orifice plate is usually chamfered on the downstream side, which must be included in the analysis because the rapidly expanding gas plume in this region often transitions to the collisionlesss regime in which the flow is not dominated by diffusion.

In the orifice, continuity dictates that the ions that hit the orifice wall are re-emitted as neutrals and re-enter the plasma. The continuity equations for the three species (neutrals, ions, and electrons) in the cylindrically symmetric orifice region are

$$\pi r^2 \left( -\frac{\partial n}{\partial t} + \frac{\partial v_o n_o}{\partial z} \right) + 2\pi r v_{\text{wall}} n = 0 \tag{6.5-5}$$

$$\pi r^2 \left( \frac{\partial n}{\partial t} + \frac{\partial v_i n_o}{\partial z} \right) - 2\pi r v_{\text{wall}} n = 0 \tag{6.5-6}$$

$$\pi r^2 \left( e\frac{\partial n}{\partial t} + \frac{\partial J_e}{\partial z} \right) = 0 , \tag{6.5-7}$$

where $v$ is the ion or neutral velocity and $v_{\text{wall}}$ is the particle velocity at the radial boundary.

The average neutral velocity is found from Poiseuille flow:

$$v_o = -\frac{r^2}{8\zeta} \frac{dP}{dz} , \tag{6.5-8}$$

where $\zeta$ is the temperature-dependent neutral gas viscosity. For xenon, the viscosity is [26]

$$\begin{aligned} \zeta &= 2.3 \times 10^{-5} T_r^{0.965} &\quad \text{for } T_r < 1 \\ &= 2.3 \times 10^{-5} T_r^{(0.71+0.29/T_r)} &\quad \text{for } T_r > 1, \end{aligned} \tag{6.5-9}$$

with units of Ns/m$^2$ or Pa-s and a relative temperature given by $T_r = T / 289.7$ K. Since a large fraction of the ions undergoes charge exchange within the orifice, the neutral gas is heated and the viscosity is increased. This is incorporated into the model [35] by assuming that the gas temperature varies as

$$T = T_{\text{wall}} + \frac{M}{k} \left[ (fv_r)^2 + v_o^2 \right], \tag{6.5-10}$$

where the fraction of the neutrals that receives the ion radial velocity via charge exchange is given by

$$f = 1 - \exp\left[-\frac{n}{n_o}\frac{\tau_{\text{wall}}}{\tau_{\text{CEX}}}\right], \tag{6.5-11}$$

and $\tau_{\text{wall}}$ is the average time between collisions with the wall for a neutral particle. This effective heating mechanism by charge exchange has been observed in experiments where the neutral temperatures are higher than the orifice wall temperatures.

Combining the electron and ion momentum equations [Eqs. (6.4-30) and (6.4-31)] to eliminate the electric field term gives an expression for the particle motion in terms of the ambipolar diffusion coefficient and the ion and electron mobilities:

$$n\left(v_i - v_o\right) = -D_a\frac{\partial n}{\partial z} + \frac{\mu_i}{\mu_e}\frac{J_e}{e}. \tag{6.5-12}$$

The ambipolar diffusion coefficient for this case is given by Eq. (6.4-4). In the orifice, the radial drift velocity will often exceed the ion thermal speed due to the radial potential gradient, so the ion scattering velocity must be approximated by

$$v_{\text{scat}} = \sqrt{v_{th}^2 + \left(v_i - v_o\right)^2 + v_r}, \tag{6.5-13}$$

where $v_r$ is the radial ion velocity found from Eq. (6.4-7).

The continuity equations in the orifice [Eqs. (6.5-5) through (6.5-7)] are solved using the electron energy equation, Eq. (6.4-28), in the cylindrical orifice, which produces ion density and plasma potential profiles in the orifice region. The first result from this work is that a double sheath postulated in the orifice region [36] is not observed for xenon ion thruster cathodes. There is a potential change through the orifice, but this results from resistive effects in the orifice channel due to electron-ion and electron-neutral collisions.

As an example, Fig. 6-20 shows a plot of the neutral and plasma densities along the axis of an NSTAR neutralizer cathode orifice operating at the TH15 power point, producing 3.76 A of current with a xenon gas flow rate of 3.5 sccm [37]. The peak plasma density occurs in the cylindrical section of the orifice, and the density falls though the chamfered region due to the neutral gas density decrease. It should be noted that the peak plasma density predicted by the 1-D model in the orifice is in reasonable agreement with the 0-D model results shown above that used the average neutral density and temperature along the length of the orifice. Reasonably accurate results can be obtained using simple 0-D models to illustrate the driving physics in this region.

An interesting result of this analysis is that significant ionization occurs in the orifice, which provides electrons to the discharge. Figure 6-21 shows the electron current calculated as a function of the distance along the orifice axis. The electron current is about 50% higher exiting the orifice as compared with the amount extracted from the insert plasma. This is because the very high neutral gas density in the neutralizer cathode orifice region causes significant ionization. Discharge cathodes have much lower electron multiplication factors in the orifice because the neutral and plasma densities are typically an order of magnitude lower.
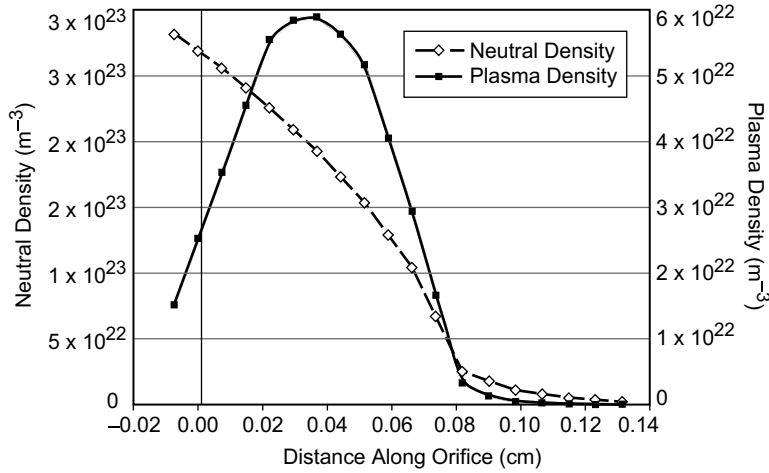


**Fig. 6-20. Neutral and plasma densities calculated in the NSTAR neutralizer cathode orifice at the TH15 operation point.**
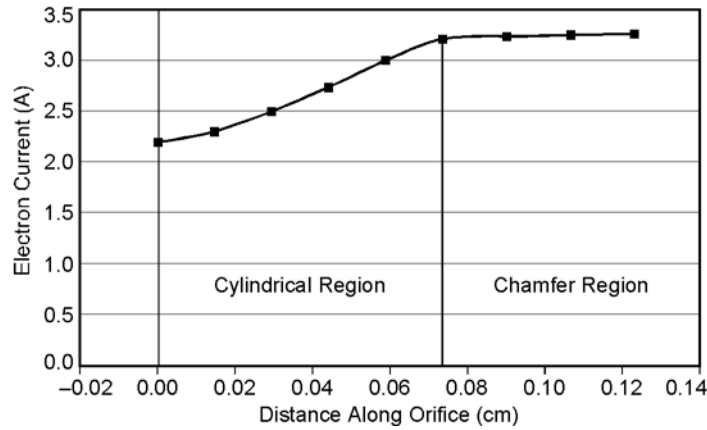


**Fig. 6-21. Electron current as a function of distance along the axis in the NSTAR neutralizer cathode orifice at TH15.**

The ion current density to the orifice wall, which naturally follows the plasma density profile in Fig. 6-20, is shown in Fig. 6-22. The ion bombardment of the orifice walls is seen to peak well before the chamfer region starts. Since the plasma potential is increasing along the axis from the insert plasma to the exit due to the plasma resistive drop, the ions in this region can have sufficient energy to sputter the wall. This effect was observed in the cross section of the NSTAR neutralizer after the 8200 life demonstration test (LDT) [34] and is shown in Fig. 6-23. The orifice was observed to open up in the center
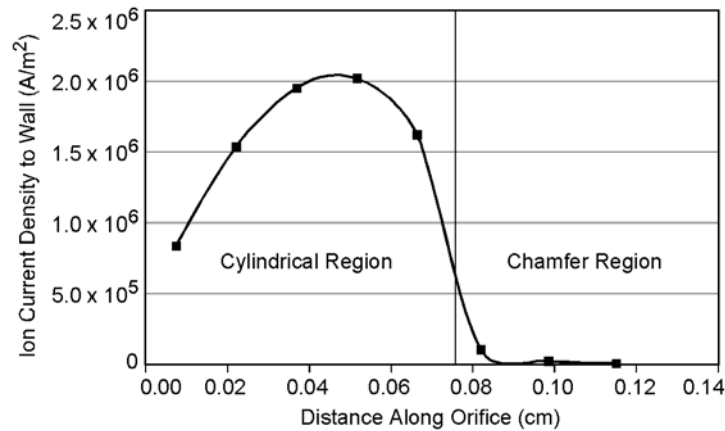


**Fig. 6-22. Radial ion current to the orifice wall as a function of distance along the axis in the NSTAR neutralizer cathode at TH15.**
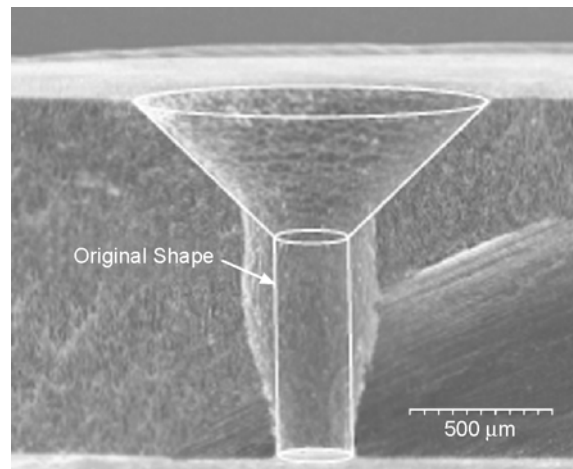


**Fig. 6-23. Neutralizer cathode orifice cross section showing the erosion pattern after the NSTAR 8200-hour test [34].**

cylindrical region before the chamfer, consistent with the predicted ion bombardment location in Fig. 6-22.

The time required to produce this erosion pattern is not known since Fig. 6-23 shows a destructive analysis after the end of the test. In fact, the erosion pattern shown in the destructive analysis of the neutralizer cathode orifice after the 30,000-hour extended life test (ELT) [38] shown in Fig. 6-24 is nearly identical to the shorter-duration LDT result. The ELT cathode experienced nearly double the operation time of the LDT cathode at the full-power level, which did not further erode the orifice. The 1-D orifice model described above finds that the larger-diameter orifice reduced the neutral pressure and plasma density in the orifice by about a factor of four, which reduced the plasma potential increase along the orifice by a factor of two. The combination of a significantly lower ion bombardment flux, the lower ion energy, and the increase in inner surface area as the cylinder radius increases caused the erosion rate to fall to negligible levels once the orifice opened sufficiently.

One might expect similar erosion behavior from discharge cathode orifices. Figure 6-25 shows the destructive analysis of the LDT discharge cathode orifice plate after 8200 hours at full power. There is no discernable erosion in the cross section. In this case, the 1-D model shows that the much larger initial orifice diameter reduced the neutral pressure, plasma density, and potential in the orifice to the point that the ion bombardment erosion became negligible (similar to the eroded neutralizer cathode orifice case). In addition, the model shows that electron multiplication is reduced due to the lower ionization rate, and so the insert plasma must produce more of the discharge current than in neutralizer cathodes. It is clear that a simple orifice-plasma model can illustrate
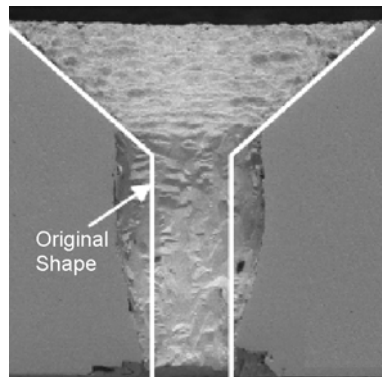


**Fig. 6-24. Neutralizer cathode orifice cross section showing the erosion pattern after the NSTAR 30,152-hour extended life test [38].**
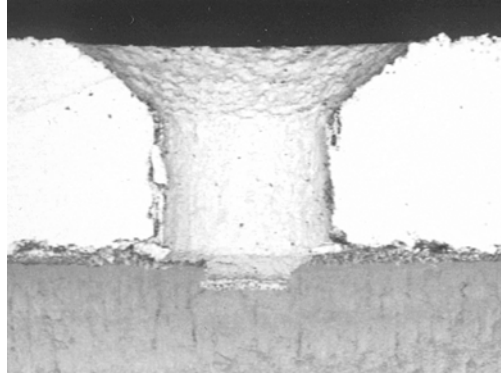
**Fig. 6-25. Discharge cathode orifice showing the erosion pattern after the NSTAR 8200-hour long duration test [34].**

the extraction and generation of the electrons in the discharge through the orifice and provide insight into the erosion mechanisms.

## 6.6  Hollow Cathode Thermal Models

While the 0-D insert model described above is illustrative, more accurate models have been constructed that use radiation and thermal conduction models coupled to 2-D insert plasma models [2] that provide the local heat fluxes. Figure 6-26 shows a sample input geometry for a 2-D cathode thermal code [30] in r–z coordinates that uses the ion and electron fluxes from the 2-D plasma codes as input to predict the temperature distribution in the cathode. In this figure, the positive numbers identify different materials, and negative numbers are used to identify radiative boundary conditions. The code includes thermal conduction, radiative heat losses, and, within the insert region, radiative heat transfer. The thermal model uses heat flux inputs calculated from the 2-D IROrCa2D plasma code [5] and includes the heating of the cathode tube and insert due to power deposition in the orifice region. Results from this code are close to the 0-D model results just described for the NSTAR cathode, but with much more accuracy and spatial resolution of the electron emission and plasma bombardment locations. Table 6-3 shows the input fluxes used in the 2-D thermal model. The plasma heating calculated by the detailed 2-D code is about 50% greater than the simple 0-D model above predicts, and most of the heat is deposited on the orifice plate.

As an example of the results from a coupled thermal and cathode plasma model, Fig. 6-27 shows the code predictions [30] and measured temperatures [33] of the insert for the NSTAR cathode running at 12 A of discharge current. The 2-D code predicts an insert temperature of about 1210°C in the first few
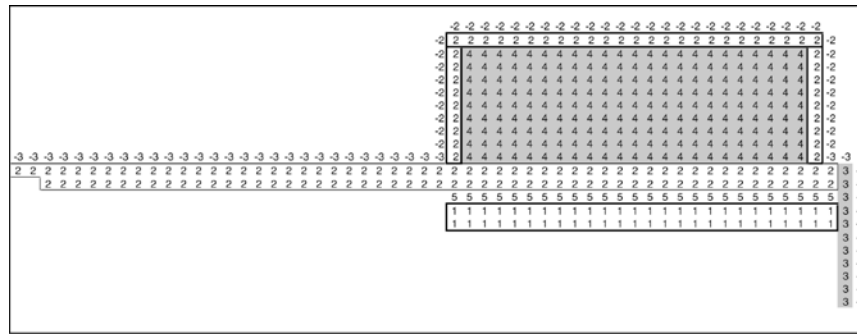
**Fig. 6-26. Hollow cathode thermal model input geometry with the different types of cells numbered and the boundary conditions indicated by numbers. Negative numbers indicate radiative boundaries [30].**
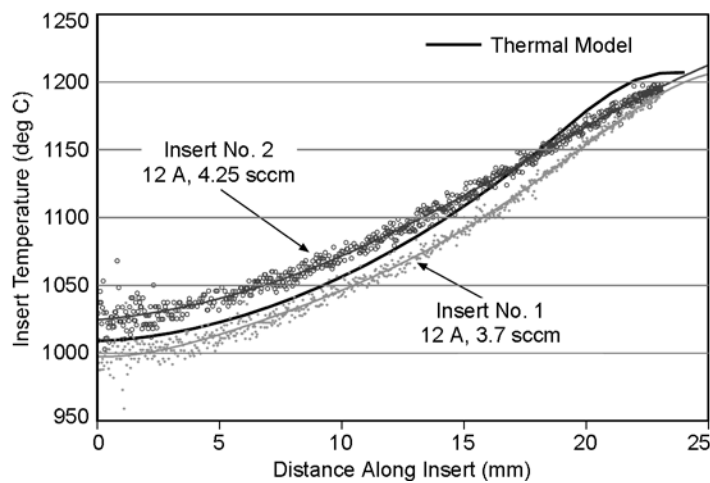


**Fig. 6-27. Comparison of the insert temperatures measured [33] and calculated for the NSTAR cathode by the 2-D coupled thermal/plasma model of Katz [30].**

**Table 6-3. Insert surface and orifice plate heating calculated using the IROrCa2D code for the NSTAR discharge cathode at 12 A and 3.5 sccm.**

| Element Heated | Power (W) |
|----------------|-----------|
| Insert Surface | 12 |
| Orifice Plate | 29 |

millimeters from the orifice plate where the plasma is in good contact with the insert. The thermal model predicts a peak temperature of about 1190°C for the heat loads from a predicted plasma contact area of 5 mm by the plasma code. The 2-D codes also show the sensitivity of the hollow cathode temperature to the emissivity of the orifice plate, the thermal contact between the emitter and

the tube, and orifice heating effects (especially in neutralizer cathodes), which impact the performance and life of the cathode. These effects cannot be obtained from the simple 0-D models used above.

## 6.7  Cathode Plume-Region Plasma

The cathode insert and orifice regions were examined above with simplified models, and this information was used to provide an understanding of the plasma parameter dependence and self-heating mechanism of the cathode. The final region of the hollow cathode to cover is exterior to the cathode orifice where the cathode plume interacts with the keeper electrode and couples the cathode emission current to the thruster discharge plasma and anode. In this region, the neutral gas expands rapidly away from the cathode and is either collisionless or makes the transition to collisionless. The electrons from the cathode are accelerated by the potential difference between the cathode orifice plasma and the plasma in the discharge chamber that is at a potential usually near the anode voltage. There is usually an applied axial magnetic field on the order of 100 G in this region to provide a transition to the ring-cusp fields in ion thrusters, which produces some confinement of the cathode plume electrons. These electrons generate the cathode plume plasma, which is also rapidly expanding away from the cathode.

The plasma stream exiting the hollow cathode is often reported as having various structures consisting of dark spaces, plasma balls, and brightly divergent plume shapes. Two of these cases are shown in Fig. 6-28, where the cathode is on the right and the anode on the left. The plasma stream consists of the electrons from the hollow cathode, neutral gas expanding from the keeper aperture in addition to more uniform background neutral gas from the thruster, and the plasma ball and stream generated by ionization of this gas by the electrons. The on-axis potential and temperature profiles measured by scanning probes for these two cases [1] are shown in Fig. 6-29. While the discharge current is the same in these two cases, the high gas flow reduced the discharge voltage from about 26 V at 5.5 sccm to 20 V at 10 sccm. The structure of the potential and temperature profiles is significantly different in the plume region as the gas flow and discharge voltage change. The higher gas flow case reduces the potentials and temperatures throughout the system and pushes the plasma ball observed at the cathode exit farther downstream.

To provide some insight into the plasma density, temperature, and potential profiles generated in this plume, a simple 1-D model [39] will be used to examine the plume physics. A full 2-D cathode plume code for the neutral gas and plasma is discussed later in this section to more accurately predict the cathode discharge behavior. The 1-D plasma model follows the same general
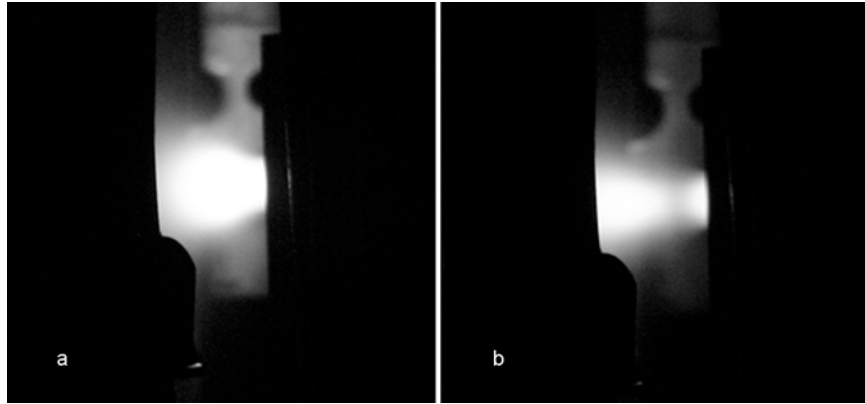
**Fig. 6-28. NEXIS cathode plume at 25 A with the plasma ball in (a) at 5.5 sccm and a dark space in (b) at high flow (10 sccm) [1].**
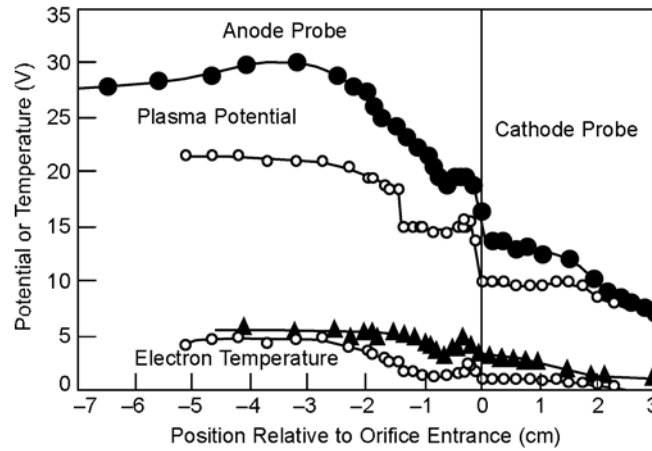


**Fig. 6-29. Plasma potential and electron temperature profiles for the two cases in Fig. 6-27, where the closed symbols are the 5.5-sccm, 26.5-V case and the open symbols are the 10-sccm, 19-V case [1].**

structure as that used for the orifice region in Section 6.5, but in this case the neutral gas is expanding and the gas and plasma flows are largely collisionless. The steady-state continuity equation is

$$0 = \nabla \cdot \left( D_a \nabla n \right) + \frac{\partial n}{\partial t},$$                (6.7-1)

where the diffusion is ambipolar with a diffusion coefficient given by Eq. (6.4-4). Using the electron momentum equation, Eq. (6.4-31), the electron current density on axis in the plume is given by

$$J_e = \frac{1}{\eta}\left(E + \frac{\nabla n T_e}{n}\right),$$
(6.7-2)

where the resistivity $\eta$ for the case of electron-neutral and electron-ion collisions in the partially ionized gas is given by Eq. (6.4-35).

The electron energy equation is given by Eq. (6.4-28) and includes convection, conduction, joule heating, pressure work, and ionization losses. Axial depletion of the neutral gas by ionization can be taken into account using a simple exponential attenuation model. The ionization rate of the neutral gas density is

$$\frac{d\,n_o}{dt} = -n_o\,n_e\,\langle\sigma_i v_e\rangle,$$
(6.7-3)

where $n_o$ is the total neutral density in the plume. The neutral density is composed of the flowing component, $n_f$, from the cathode and the background neutral density in the chamber, $n_c$:

$$n_o = n_f(z) + n_c.$$
(6.7-4)

The density of the flow gas decreases with distance away from the cathode orifice:

$$\frac{d\,n_f(z)}{dz} = \frac{1}{v_o}\frac{d\,n_f}{dt} = \frac{1}{vo}\left(\frac{d\,n_o}{dt} - \frac{d\,n_c}{dt}\right),$$
(6.7-5)

where $v_o$ is the neutral gas velocity. Using Eq. (6.7-3), Eq. (6.7-5) can be written as

$$\frac{1}{n_f(z)}\frac{d\,n_f(z)}{dz} = -\frac{1}{v_o}n_e\,\langle\sigma_i v_e\rangle,$$
(6.7-6)

which has a solution of the flow density decreasing exponentially away from the cathode. This is the same as the case analyzed in Section 3.6, in which the ionization mean free path is found to be one over the right-hand side of Eq. (6.7-6).

The above equations [Eqs. (6.7-1) through (6.7-6)] are solved in a simple computational mesh shown in Fig. 6-30. The neutral gas is assumed to expand with a full angle of 45 deg. The code has been used to solve for the NEXIS

cathode density and potential profiles at the standard operating condition of 25-A and 5.5-sccm xenon gas flow. The density profile is shown in Fig. 6-31, where the agreement between the 1-D model and the data is reasonably close. The plasma potential and electron temperature profiles are shown in Fig. 6-32, where the agreement is reasonably good. Of interest is the fact that the electron Mach number (electron drift velocity divided by the thermal velocity) is well below 1, indicating that double layers and streaming instabilities are not expected for this case. The visual observation of the cathode plume with a
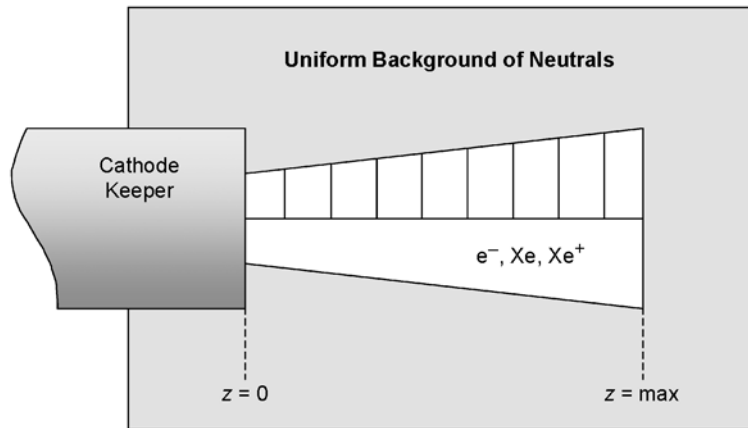


**Fig. 6-30. Computational region for the 1-D cathode plume model [39].**
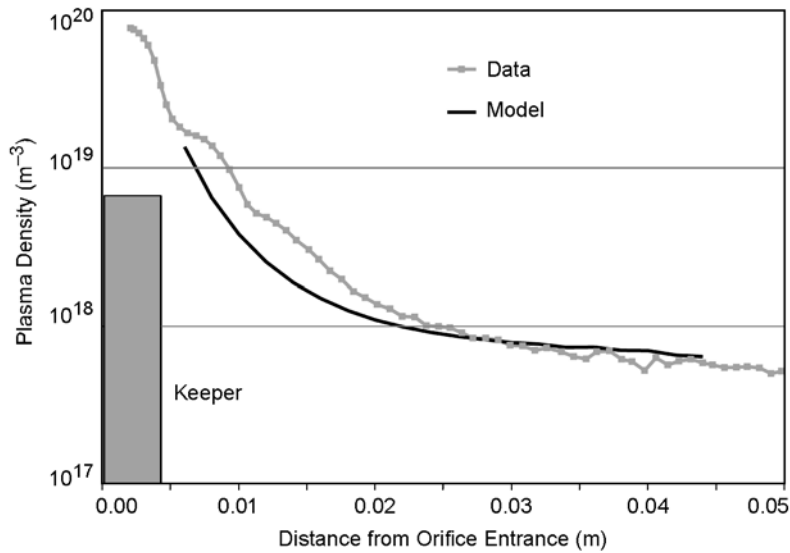


**Fig. 6-31. Density profile from the 1-D model and the axial probe data for the NEXIS cathode plume plasma density at 25 A and 5.5 sccm [39].**
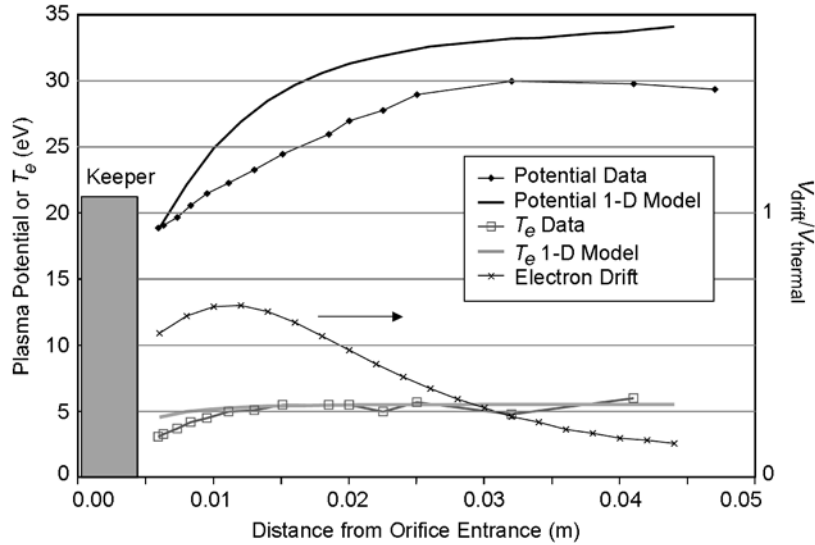
**Fig. 6-32. Potential and temperature profiles from the 1-D model and the axial probe data from the NEXIS cathode at 25 A and 5.5 sccm [39].**

bright, well defined "plasma ball" shown in Fig. 6-28 might suggest potential or density discontinuities, but this is not the case. The fact that the plasma density is falling exponentially away from the keeper, and that the neutral gas density falls as the inverse distance from the cathode squared as well, suggests that the boundaries of the ball are just the manifestation of a rapidly decreasing excitation rate and the visual integration of transverse chords through this 3-D region by the eye.

The plasma potential and electron temperature profiles for the case of the NEXIS cathode at 25 A with a higher gas flow (10 sccm) are shown in Fig. 6-33. In this case, close to the keeper, the potential and temperature predicted by the model do not agree well with the data, and the photograph in Fig. 6-28(b) suggests a dark space in this region of very low electron temperature that is not captured by the 1-D model. However, the potential discontinuity or jump observed in the experimental data for this case at about 1 cm from the keeper exit corresponds to an electron temperature increase and higher plasma potentials. In the lower temperature region upstream of this potential jump, the model indicates that the electron Mach number is approaching 1, which suggests the generation of a double layer or plasma instabilities that accelerate the electrons and heat the plasma.

Double layers can be formed in regions where the plasma potential changes rapidly between two relative low-field regions. Double layer formation was originally analyzed by Langmuir [40] and was described in Chapter 3. Across
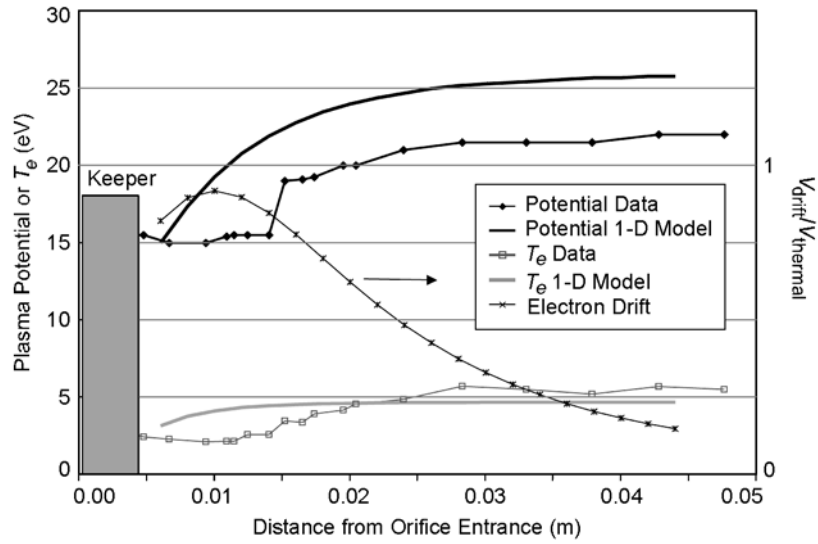
**Fig. 6-33. Potential and temperature profiles from the 1-D cathode plume model and the axial probe data for the NEXIS cathode at 25 A and 10 sccm [39].**

the double layer, the ion and electron charge densities integrate to zero. The relationship between the ion and electron currents flowing across the layer is given by

$$J_e = k \sqrt{\frac{M}{m}} J_i, \tag{6.7-7}$$

where $k$ is a constant that is about 0.5 for $T_e / T_i \approx 10$. The double layer forms if the electron drift speed exceeds the electron thermal speed. This can occur if the ionization rate in the plume along the current path drops and there is insufficient plasma generated to support the discharge current. In this case, the double layer accelerates the electrons to higher energies, which increases the ionization rate.

The axial location of a double layer can be found by finding the location along the cathode plume where Eq. (6.7-7) is satisfied. Assuming that the neutral gas expands at a fixed cone angle, the tangent of which is the half angle $\alpha$, the neutral density along the plume is

$$n_o(z) = \frac{Q_{\text{gas}}}{v_o \pi (r + \alpha z)^2} . \tag{6.7-8}$$

If the ions are generated by the accelerated electrons within about one local radius downstream of the double-layer flow back through the double layer, the ion current is

$$I_i \approx I_e \int_z^{z + r_o + \alpha z} \sigma_i n_o(z) dz .$$

(6.7-9)

Substituting Eq. (6.7-8) into Eq. (6.7-9) and integrating, the ion current through the sheath is

$$I_i = I_e \frac{Q_{\mathrm{gas}} \sigma_i}{v_o \pi} \frac{1}{(r_o + \alpha z)} \frac{1}{(1 + \alpha)} .$$

(6.7-10)

Defining the "Langmuir ratio" from Eq. (6.7-7) as

$$R_L \equiv \frac{J_i}{2 J_e} \sqrt{\frac{M}{m}} ,$$

(6.7-11)

a stable double layer will form in the location where $R_L$ equals one. Using Eq. (6.7-10), the Langmuir ratio is

$$R_L = \frac{2 Q_{\mathrm{gas}} \sigma_i}{v_o \pi} \sqrt{\frac{M}{m}} \frac{1}{(r_o + \alpha z)} \frac{1}{(1 + \alpha)} .$$

(6.7-12)

In the cathode plume, Eq. (6.7-12) indicates that the Langmuir ratio decreases monotonically with distance from the cathode. Alternatively, the axial location where the Langmuir condition equals 1 can be found to identify the location of the double layer. This is shown in Fig. 6-34 where the flow rate at which $R_L = 1$ is plotted versus distance from the cathode orifice. At flow rates of 10 sccm, Fig. 6-34 suggests that a double layer will form over 1-cm downstream from the cathode, consistent with the data shown in Fig. 6-33. The general behavior of the double-layer location moving axially downstream with increasing gas flow has been reported [1] by both visual observations and by probe measurements.

The cathode plume is much more complicated than this simple 1-D model suggests, and the condition of increasing electron-Mach numbers predicted under certain situations by the 1-D code may generate double layers or instabilities in the plasma not well described by the fluid codes. The assumed neutral gas expansion behavior and the associated electron current density in the plume were fortuitously picked to give potential and density profiles that came close to matching the experimental data. In reality, the neutral gas likely expands more rapidly than the 45-deg cone assumed in the 1-D model. The low
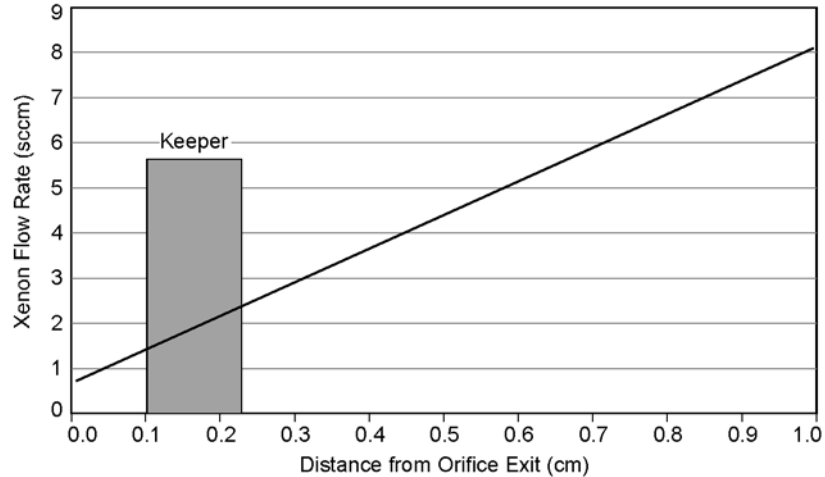
**Fig. 6-34. Flow rate at which the Langmuir ratio is equal to one and double layers can be formed as a function of the distance downstream from the NEXIS cathode orifice [39].**

electron temperature obtained from classical resistivity, with the low neutral density in the plume, produce insufficient ionization to generate the required plasma density to match the experimental data and carry the current to the anode. This situation leads to the increase in the local electron Mach number and the possible generation of double layers described above or to plasma instabilities that increase the resistivity anomalously and heat the electrons to produce more ionization.

A full 2-D model of the cathode plume is under development at the Jet Propulsion Laboratory (JPL) to investigate these issues [41]. The OrCa2D code uses a 2-D neutral gas fluid code in the insert and cylindrical orifice regions and then transitions to a collisionless neutral gas model from the orifice chamfer region into the plume. This provides the correct neutral gas density profile in the cathode plume region high numerical accuracy. The 2-D plume code then extends the system of equations used in the 2-D orifice model previously described in Section 6.4 [Eqs. (6.4-28) through (6.4-35)] on an adaptive mesh to provide the resolution required near the keeper and minimize the computational time. In solving the above equations, the code also addresses the onset of instabilities as the Mach number approaches one that produces anomalous resistivity and electron heating. For example, Fig. 6-35 shows the plasma density profile calculated by the code for the NEXIS cathode operating at the nominal 25 A and 5.5 sccm for the case of classical and anomalous resistivity in the cathode plume. The use of the classical resistivity given in Eq. (6.4-35) results in a low electron temperature in the plume region and insufficient ionization to match the experimental plasma density profile.
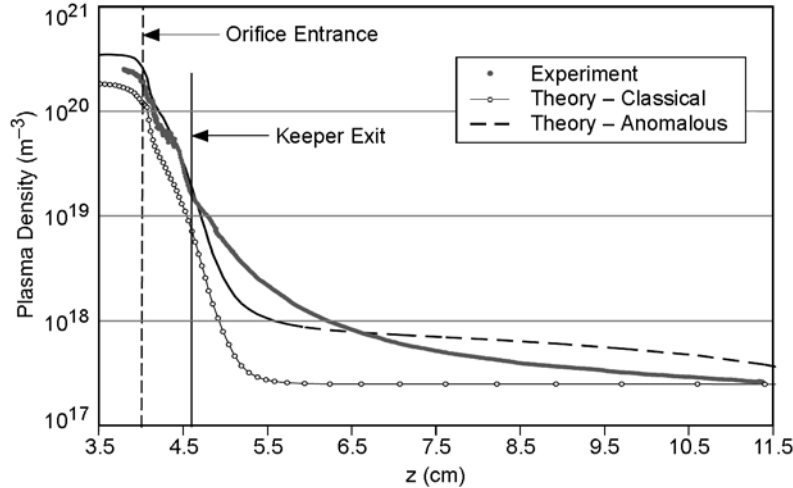
**Fig. 6-35. Plasma density profile on axis for the NEXIS cathode showing that an anomalous resistivity is required to provide sufficient ionization to come close to matching the experimental data [41].**

Incorporating anomalous resistivity associated with the generation of ion acoustic instabilities in the cathode plume provides higher electron temperatures and more ionization in the plume, which better matches the measured profiles. Additional work is required to complete this model, but as the model development progresses, a clearer picture of the cathode plume physics will result.

The 2-D structure of the cathode plume as it expands from the cathode orifice has been investigated by several authors [28,31,42]. Figure 6-36 shows plasma density contours measured [43] with a fast scanning Langmuir probe. The density is the highest on axis and closest to the cathode orifice, which is consistent with the visual appearance of a bright cathode ball or spot at the cathode exit that expands both radially and axially into the discharge chamber [28]. A reduction in cathode gas flow causes the ball or spot to pull back toward the cathode orifice and the plasma to expand into what is called a plume mode [44,45]. Plume mode operation generally results in high-frequency oscillations in the cathode plume that propagate into the discharge chamber and keeper region, and can couple to the power supply leads if of sufficient amplitude. The plasma potential contours measured in this case by the probe are shown in Fig. 6-37. The potential is actually a minimum on axis near the cathode, and then increases radially and axially away from the cathode exit to a value several volts in excess of the discharge voltage [28,43]. This structure near the cathode is sometimes called the trough because ions generated externally to the cathode tend to funnel into the trough and toward the cathode. Large amplitude plasma
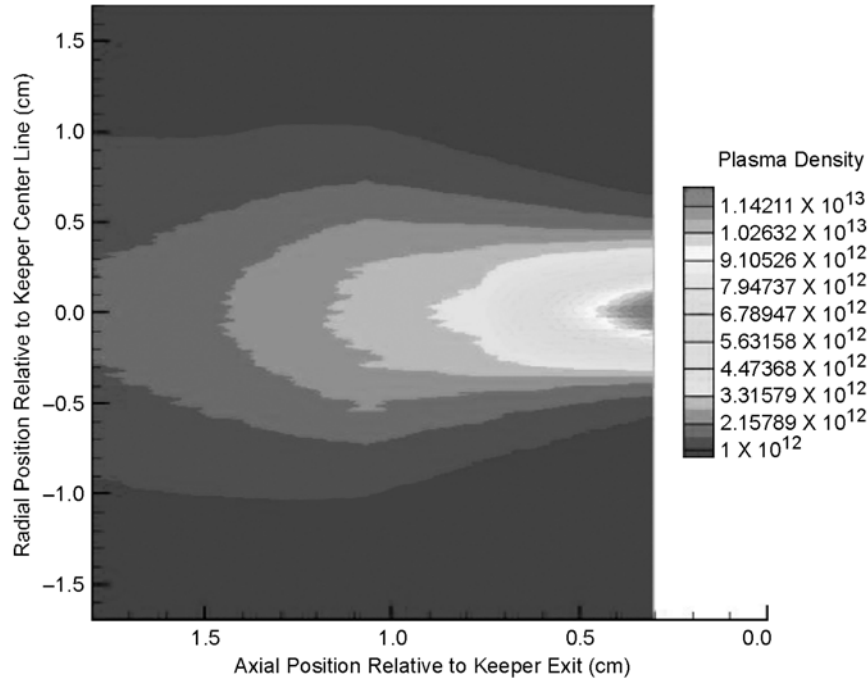
**Fig. 6-36. Plasma density contours measured for the NEXIS cathode at the nominal 25-A and 5.5-sccm gas flow discharge condition [43].**

potential oscillations in the range of 50–1000 kHz have been observed primarily in and around the edge of the plasma ball and in front of the keeper electrode from high-speed scanning emissive probes [46]. These may be the result of the increased Mach number and instabilities described above under certain conditions.

## 6.8  Hollow Cathode Life

Cathode insert life is fundamentally determined either by depletion of the BaO emissive mix impregnated into the dispenser cathodes so that the surface work function is degraded or by evaporation of the emissive material in refractory metal cathodes, such as tungsten and tantalum, and in crystalline cathodes, such as $LaB_6$. The cathode mechanical structure (orifice plate, heater, cathode tube, etc.) also can be worn out or degraded by ion-induced sputtering, which affects the cathode life. The impact on the cathode performance by these two life-limiting fundamental mechanisms is important to understand in designing cathodes for ion and Hall Thrusters. In addition, poisoning of inserts due to impurities in the feed gas or improper exposure to air also can increase the work function and impact cathode life.
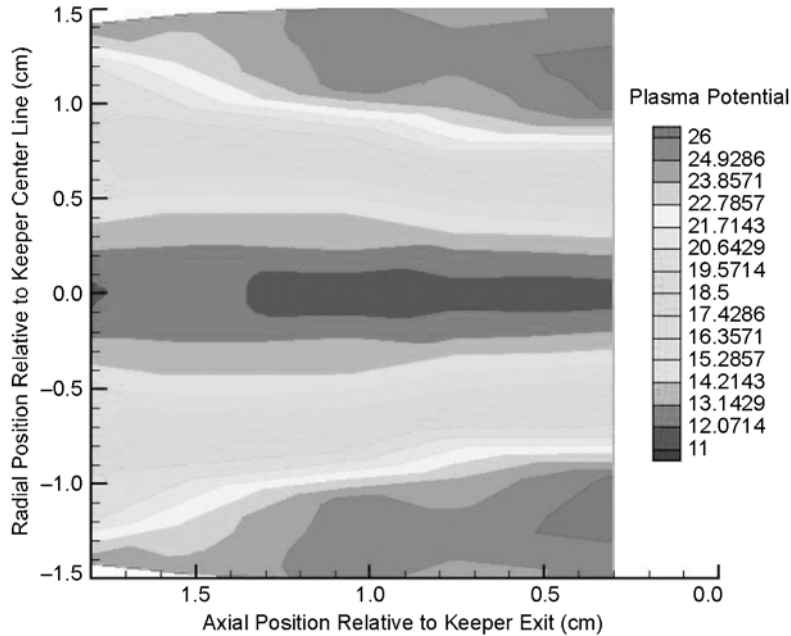
**Fig. 6-37. Plasma potential contours measured for the NEXIS cathode at the nominal 25-A, 5.5-sscm discharge condition [43].**

## 6.8.1 Dispenser Cathodes in Insert Plasmas

In dispenser cathodes, evaporation of the barium layer coating the cathode surface is well understood, and depletion life models can be readily constructed if this is the root cause of barium loss [47]. However, the emitter surface is exposed to a plasma, and ion bombardment of the surface by ions from the insert-region plasma can increase the loss of barium from the surface, which will reduce the lifetime of the cathode. While the basic concept of a hollow cathode is to reduce the erosion and modification of the low work-function insert surface with a high-pressure, collisional insert plasma, this benefit had to be validated before the cathode life could be predicted [47].

An experimental and theoretical study of enhanced barium evaporation from dispenser cathode surfaces was undertaken [48] to determine the plasma conditions in the insert region under which an evaporation model could be used. The experimental arrangement measured the barium evaporation from a Type S 4:1:1-impregnated porous tungsten cathode with an embedded heater during xenon plasma bombardment. The cathode could be biased negatively relative to the plasma in order to control the ion bombardment energy. The barium evaporation rate was measured by a fiber optic coupled to a visible wavelength spectrometer tuned to detect the emission intensity of the Ba-I line

at 553.5 nm excited in the plasma. Since the emission intensity depends on the amount of Ba present in the plasma and the electron density and temperature, the plasma parameters were monitored with a probe and the Ba-I signal was normalized to a neutral xenon line to account for any variations in plasma parameters during the measurements.

Figure 6-38 shows the barium loss rate measured at 725°C versus the ion bombardment energy. Increasing the ion bombardment energy from 10 to 30 eV increases the barium loss rate by an order of magnitude. Figure 6-39 shows the barium loss rate as a function of temperature for two cathode bias energies. For the case of the cathode floating relative to the plasma, the ion bombardment energy is only a few eV and the barium loss rate is determined solely by thermal evaporation. For a bias energy of 15 eV, the barium loss rate is found to be the same as for thermal evaporation for cathode temperatures in excess of about 800°C. Since the hollow cathodes in most thrusters operate at insert temperatures in excess of 1000°C, these data show that the barium loss rate is determined by thermal evaporation rates.

A model of the enhancement of barium evaporation for a surface under energetic ion bombardment was developed by Doerner, et al. [49] to explain this behavior. At elevated surface temperatures, two classes of surface particles must be considered at the surface: (a) those particles that are bound to the material lattice structure (denoted here as "lattice atoms") and (b) atoms that have been liberated from the lattice structure, but which are still bound to the
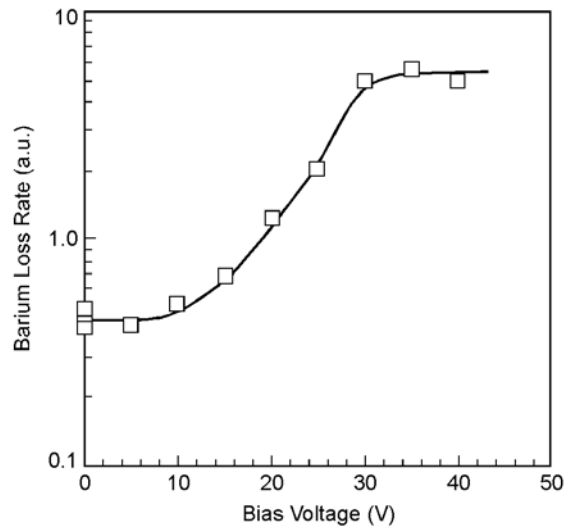


**Fig. 6-38. Variation of barium loss rate from the cathode surface at 725°C with cathode bias voltage (redrawn from [48]).**
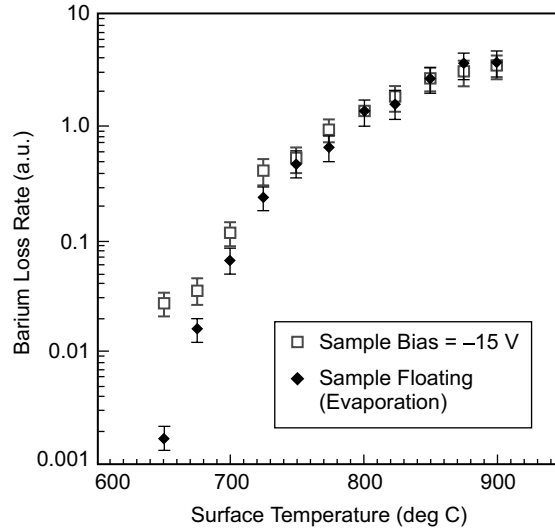
**Fig. 6-39. Relative Ba concentration in Xe plasma for
two bias conditions (redrawn from [48]).**

material surface with a reduced binding energy (denoted here as "adatoms"). Both species can sublimate from the material surface if an atom receives enough kinetic energy from random collisions to break free from the surface; however, because the binding energy for the two species is different, the corresponding loss rate also will be different.

The net flux of material from the surface can be written as

$$J_T = J_i Y_{\text{ps}} + K_o n_o \exp^{(-E_o / T)} + \frac{Y_{\text{ad}} J_i}{\left(1 + A \exp^{(E_{\text{eff}}/T)}\right)} , \qquad (6.8\text{-}1)$$

where $J_i$ is the plasma ion flux, $Y_{\text{ad}}$ is the adatom production yield from the incident ion flux, $Y_{\text{ps}}$ is the sputtered particle yield, and $Y_{\text{ad}} J_i$ is equal to the adatom loss rate due to both sublimation and recombination. The first term in Eq. (6.8-1) describes physical sputtering of lattice atoms (which is independent of surface temperature); the second term describes the thermal sublimation of lattice atoms, which is independent of ion flux; and the third term describes the losses due to adatom production and subsequent sublimation, which depends upon both the incident ion flux and the surface temperature. For Xe ions incident on BaO at 30 eV, $Y_{\text{ps}} = 0.02$, $A = 2 \times 10^{-9}$, and

$$\frac{Y_{\text{ad}}}{Y_{\text{ps}}} \approx 400 . \qquad (6.8\text{-}2)$$

These parameters can be used to model the expected net flux of Ba from a surface under bombardment with 30-eV Xe ions for various surface temperatures. The result of this model is compared with experimental measurements of Ba emissivity under these conditions in Fig. 6-40. The model compares extremely well with the experimental results. The model also qualitatively explains the key experimental observations, including the effect of ion energy on net erosion, the saturation of the adatom loss term at elevated temperatures, and the transition to losses dominated by thermal sublimation of lattice atoms at elevated temperatures. The model has been used to examine the effect of increasing the ion flux to the surface from the values in these experiments to the actual values for the hollow cathodes found from the 2-D plasma model. In this case, the model predicts that thermal evaporation dominates the barium loss rate for ion energies of less than 15 eV and cathode temperatures of over 900°C. The model provides confidence that the barium loss rate effects in the plasma are understood and that the main result of barium loss determined by thermal evaporation rates for the plasma parameters of thruster cathodes examined here is accurate.

## 6.8.2   Cathode Insert Temperature

Since the barium evaporation rate for the plasma conditions found in the hollow cathodes is determined by the insert surface temperature, a non-contact temperature measurement technique was developed at JPL [50] to directly measure the insert temperature during cathode operation. The technique
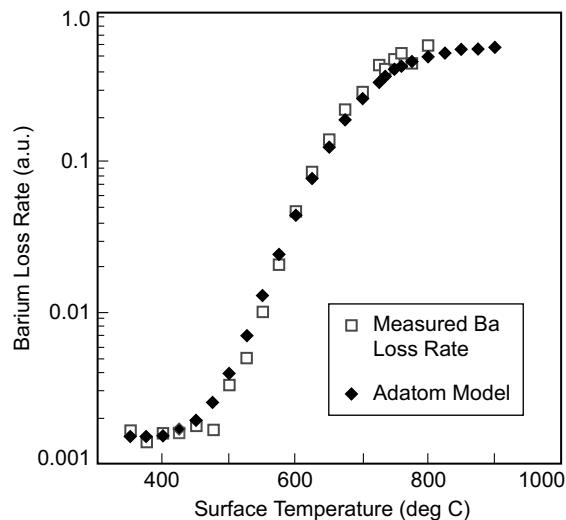


**Fig. 6-40. Ba concentration versus cathode surface temperature for −15 V bias. Experimental data are shown by open squares and the model prediction are shown by the diamonds (from [48]).**

employs a stepper-motor-driven sapphire fiber-optic probe that is scanned along the insert inside diameter and collects the light radiated by the insert surface. Ratio pyrometry is used to determine the axial temperature profile of the insert from the fiber-optic probe data. Thermocouples attached on the outside of the cathode on the orifice plate provide additional temperature data during operation and are used to calibrate the pyrometer system in situ with a small oven inserted over the cathode to equilibrate the temperature.

Figure 6-41 shows temperature profiles measured for a nominal Space Station Contactor (SSC) cathode [50] operating at four different discharge currents. The peak temperature of the insert at the full 12-A current level is about 1200°C. The insert also has approximately a 10% to 15% temperature gradient along its length. The change in the insert temperature with the xenon flow rate for the cathode producing 12 A of discharge current is shown in Fig. 6-42. High flow rates through the cathode reduce the insert temperature, although the effect is small.

A direct comparison of the insert temperature profile for the NSTAR discharge cathode and the SSC cathode at identical discharge currents of 12 A and xenon flow rates of 6 sccm is shown in Fig. 6-43. The NSTAR insert temperature is higher than the SSC all along the insert. It also appears that the temperatures of the inserts tend to converge near the orifice plate. The high insert temperature for the NSTAR cathode is likely because the plasma contact area is significantly larger at the roughly 50% lower internal pressure as compared with the SSC. In addition, thermocouple measurements on the orifice plate show that the smaller-diameter SSC orifice plate is significantly hotter than the NSTAR orifice plate, consistent with orifice heating effects described in Section 6.5 for smaller orifice diameters.
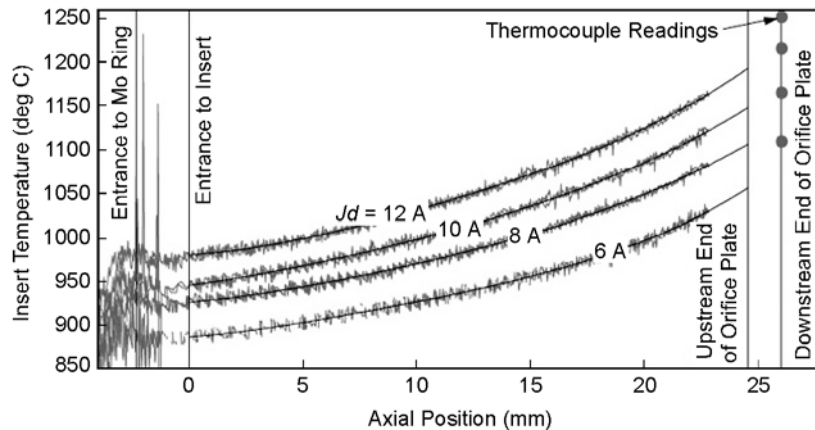


**Fig. 6-41. Insert temperature profile measured for a SSC hollow cathode for several different discharge currents (from [50]).**
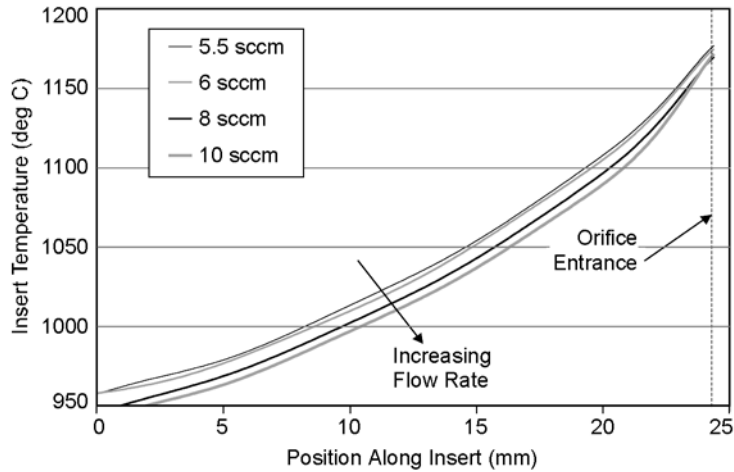
**Fig. 6-42. Insert temperature profile for an SSC hollow cathode operating at 12 A of current for several different gas flow rates (redrawn from [50]).**
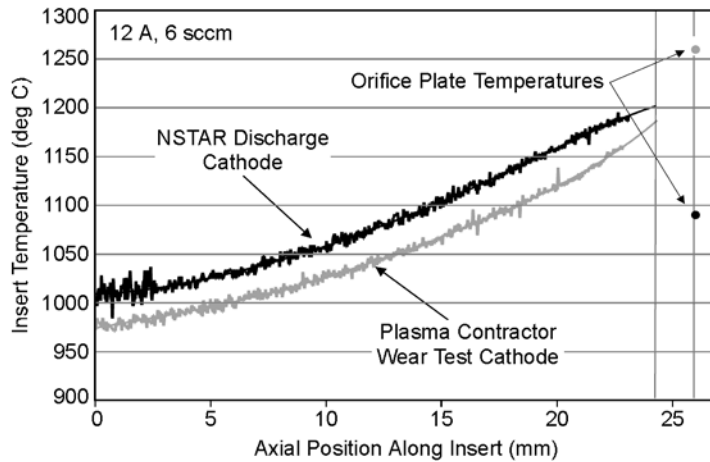


**Fig. 6-43. Comparison of the insert temperature profile for the Space Station Contactor cathode and the NSTAR discharge cathode at 12 A (from [33]).**

### 6.8.3 Barium Depletion Model

The previous sections showed that the barium loss rate from hollow cathode dispenser cathode inserts should be essentially the same as dispenser cathode inserts operated in vacuum if the ion bombardment energy is sufficiently low in the hollow cathode. Since plasma potentials on axis in the insert plasma of less than 15 V are routinely measured [1,28] and sheath potentials of less than 10 V

are found from the models discussed above, the insert life will be limited by evaporation in the same manner as in vacuum devices.

Published measurements by Palleul and Shroff [51] of the depth of barium depletion in dispenser cathodes as a function of time and temperature show that barium depletion obeys a simple diffusion law with an Arrhenius dependence on temperature. This is shown in Fig. 6-44 (from [51]), where the impregnate surface layer in the pore recedes with time. The "activation energy" in the diffusion coefficient that determines the slope of the curves in Fig. 6-44 appears to be relatively independent of the cathode type.

From data presented in Fig. 6-44, the operating time to deplete impregnate from the insert material to a depth of 100 μm is

$$\ln \tau_{100\,\mu\mathrm{m}} = \frac{eV_a}{kT} + C_1 = \frac{2.8244e}{kT} - 15.488 , \qquad (6.8\text{-}3)$$

where the operating time $\tau_{100\,\mu\mathrm{m}}$ is in hours, $e$ is the elementary charge, $V_a$ is the activation energy, $k$ is Boltzmann's constant, $C_1$ is a fit coefficient, and $T$ is the insert temperature in kelvins. The activation energy was found from Fig. 6-44. Using this relationship and the fact that the depletion depth is
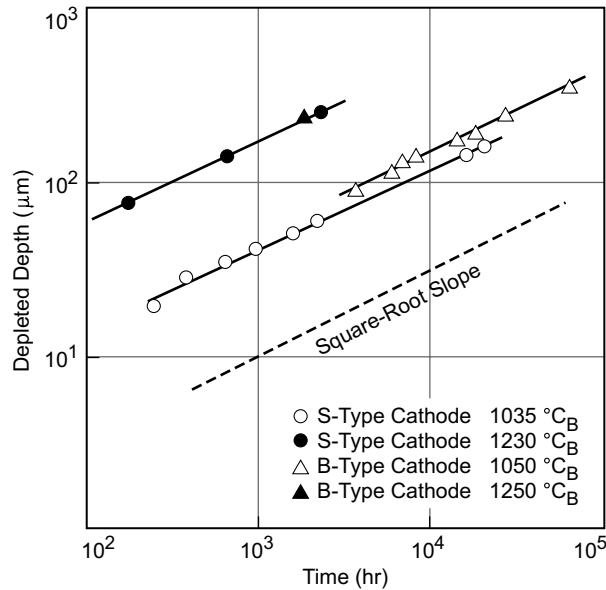


**Fig. 6-44. Depletion depth of a porous tungsten insert as a function of time for cathodes at different temperatures (redrawn from [51]).**

proportional to the square root of the operating time [51], an equation yielding the insert lifetime due to barium depletion can be derived [47]:

$$\tau_{\text{life}} = \tau_{100\mu\text{m}} \left( \frac{y}{y_{100\mu\text{m}}} \right)^2, \tag{6.8-4}$$

where $\tau_{100\,\mu\text{m}}$ is the time to deplete to 100 µm in depth from Eq. (6.8-3), $y$ is the insert thickness in µm, and $y_{100\mu\text{m}}$ is the 100-µm reference depth. Using Eq. (6.8-3) in Eq. (6.8-4), the life of a Type S dispenser cathode in hours is

$$\tau_{\text{life}} = 10^{-4} y^2 \exp\left( \frac{2.8244e}{kT} - 15.488 \right), \tag{6.8-5}$$

where $y$ is the insert thickness in µm and $T$ is the insert temperature in kelvins. Figure 6-45 shows the insert life for a 1-mm depletion depth versus the insert temperature. Insert life of over 100,000 hours is readily achievable if the insert is thick enough. At around a nominal 1100°C operating temperature, the life increases a factor of 2 if the temperature decreases 40°C.

This model represents a worst-case estimate of the cathode life. In very high-density hollow cathodes, like the NSTAR cathode, the ionization mean free path for the evaporated barium is significantly less than the insert plasma radius. This means that a large fraction of the barium is ionized close to the insert surface. The electric field in this region is primarily radial, which means that some large fraction of the barium is recycled back to the surface. The barium surface coverage is then partially re-supplied by recycling, which can extend the life considerably.
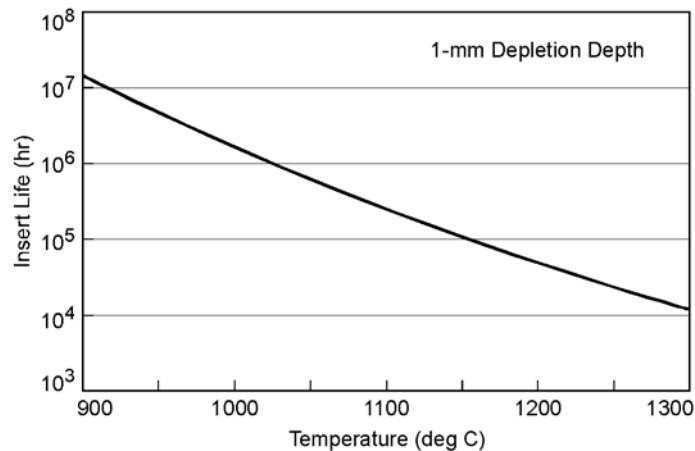


**Fig. 6-45. Insert life from barium evaporation calculated for a 1-mm depletion depth versus temperature.**

To predict cathode life in a thruster application from an insert depletion mechanism, a relationship between the insert temperature and the discharge current at a given gas flow must be obtained. The SSC insert temperature was measured versus discharge current by Polk [50]. These data are well fit in the plasma contact region (the 3 mm closest to the orifice plate) by

$$T = 1010.6 \, I_d^{0.146} [\text{K}]. \tag{6.8-6}$$

At 12 A of discharge current, this gives an insert temperature of 1453 K. Since the insert in this cathode is about 760-µm thick and we assume that the insert is depleted when the depth reaches about two-thirds of the thickness (due to some barium diffusion out the outside diameter of the insert), Eq. (6.8-5) predicts a life of 30,000 hours. This is in good agreement with the SSC life test data where the cathode failed to start after about 28,000 hours at 12 A of discharge current [52]. In this case, barium recycling may not affect the insert life significantly because the plasma is in contact with the insert for only a couple of millimeters, from the orifice plate, and the barium will tend to migrate to regions that are not involved in the emission process.

For the NSTAR cathode, the insert temperature data as a function of discharge current measured by Polk [33] are well fit in the plasma contact region by

$$T = 1191.6 \, I_d^{0.0988} [\text{K}]. \tag{6.8-7}$$

At the full-power discharge current of 13 A, and using the insert thickness of 760 µm, Eq. (6.4-5) predicts an insert life of 20,000 hours. The ELT ran at full power for about 14,000 hours and accumulated an additional 16,352 hours at much lower discharge currents [53]. The barium depletion model indicates that the insert should have been depleted in the emission zone in less than 24,000 hours. Measurements indicate partial depletion in the emission region near the orifice, but that as much as 30% of the original barium was still present [53]. Clearly barium recycling in the plasma reduced the effective evaporation rate and extended the life of the cathode significantly.

For the NEXIS hollow cathodes, the operating insert temperature profile has not yet been measured. Estimates of the insert temperature were made using an early version of the combined plasma and thermal model [47]. Since the discharge loss and efficiency performance of the NEXIS thruster are known, the relationships in Chapter 2 can be used to plot thruster life versus engine performance. The NEXIS thruster operates at 75% to 81% efficiency over an Isp of 6000 to 8000 s [54]. Figure 6-46 shows the model-predicted depletion-limited life of this insert versus specific impulse for several thruster power levels. At the nominal operating point of 7000 s Isp and 20 kW, the cathode is
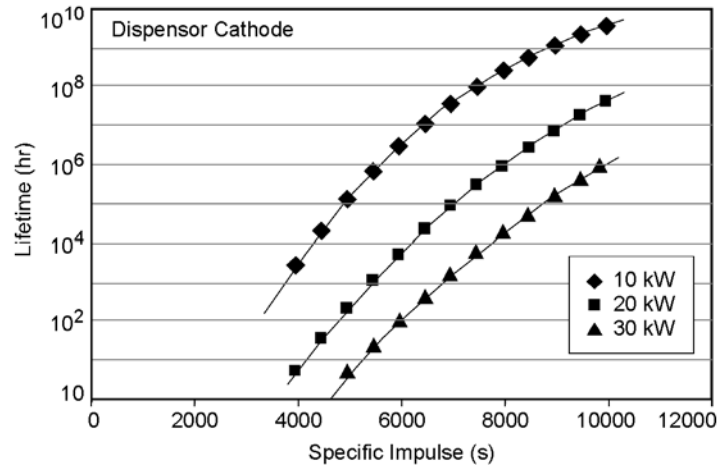
**Fig. 6-46. Model prediction of NEXIS dispenser cathode life versus Isp for several thruster powers [47].**

projected to operate for about 100,000 hours. Increasing the Isp requires operation at higher beam voltages, which for a given power requires less beam current and, thereby, less discharge current. A lower discharge current reduces the insert temperature for a given cathode size, which reduces the barium evaporation rate and extends the cathode life. Likewise, lower Isp and higher power require higher discharge currents, which translate to a reduction in the cathode life. It should be noted that the cathode life in Eq. (6.8-5) scales as the insert thickness squared, so the life at any operating point in Fig. 6-46 can be extended simply by increasing the thickness of the insert. This may require increases in other dimensions, but proper selection of the cathode diameter and orifice size can be made to maintain the insert temperature at the desired level to provide the desired life.

### 6.8.4 Bulk-Material Insert Life

Cathodes that are based on bulk insert material instead of dispenser chemistry, such as $LaB_6$, have a lifetime that is determined by the evaporation of the insert material inside the hollow cathode [18]. In plasma discharges, sputtering of the $LaB_6$ surface can also impact the life [22]. However, as in dispenser hollow cathodes, the plasma potential is very low in the insert region and the bombardment energy of xenon ions hitting the surface is typically less than 20 V, which virtually eliminates sputtering of the cathode surface. It is assumed that the evaporated material leaves the cathode and does not recycle to renew the insert surface, which will provide a lower estimate of the insert life than might actually exist. Interestingly, as the insert evaporates, the inner diameter increases and the surface area enlarges. This causes the required current density

and temperature to decrease at a given discharge current, which reduces the evaporation rate of the insert with time.

The life of the $LaB_6$ insert for three different cathode diameters versus discharge current was calculated based on the evaporation rate at the temperature required to produce the discharge current in the thermally limited regime [18]. Assuming that 90% of the insert can be evaporated, the cathode life is shown in Fig. 6-47 as a function of the discharge current. Lifetimes of tens of thousands of hours are possible, and the larger cathodes naturally tend to have longer lives. While other mechanisms, such as temperature variations along the insert, $LaB_6$ surface removal, or material build-up due to impurities in the gas, can potentially reduce the life, redeposition of the evaporated $LaB_6$ material will tend to extend the cathode life. Therefore, these life estimates for the different cathode sizes are mostly valid relative to each other, and the actual lifetime of the cathode can be considered to be on the order of the values shown in Fig. 6-47.

To obtain an idea of the lifetime of a $LaB_6$ cathode relative to a conventional dispenser cathode, the predictions from a dispenser cathode life model [47] applied to the NSTAR cathode are compared with the 0.8-cm $LaB_6$ cathode life predictions in Fig. 6-48. These two cathodes have similar insert diameters and lengths, and so a direct comparison is possible. The dispenser cathode calculation assumes that barium evaporation from the insert surface causes depletion of nearly all of the barium impregnate at the end of life in the NSTAR dispenser cathode at the measured [33] insert temperature and temperature gradient. This provides an upper limit to the dispenser cathode life if other
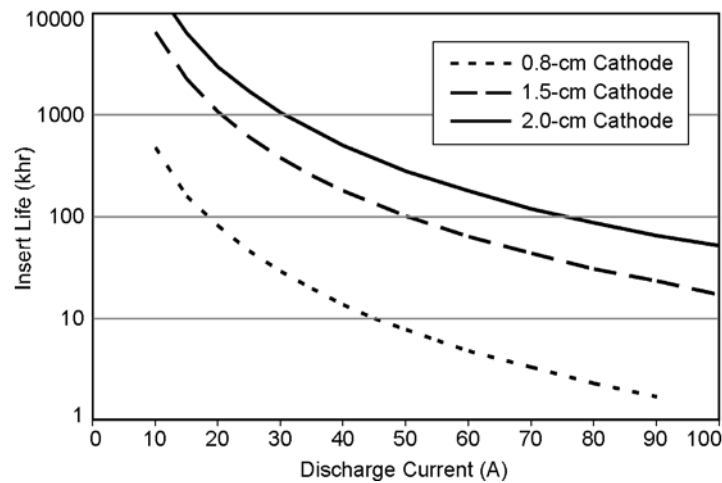


Fig. 6-47. Calculated lifetime in thousands of hours versus the discharge current for three different $LaB_6$ cathode diameters.
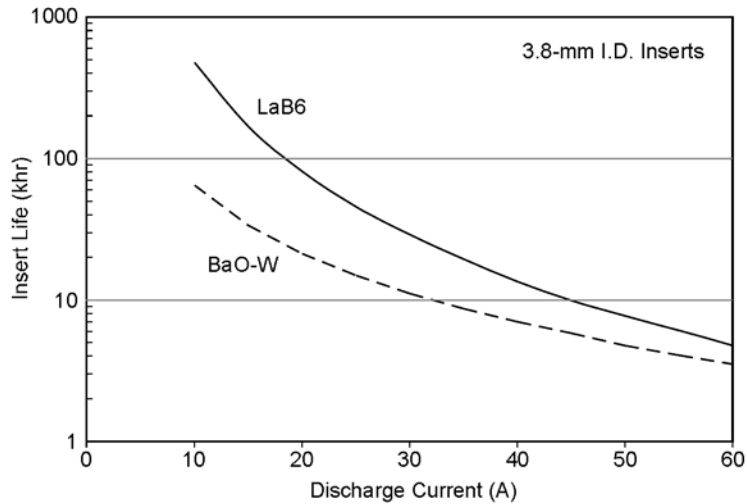
**Fig. 6-48. Comparison of the calculated cathode lifetime versus the discharge current for the 0.8-cm outside diameter LaB6 cathode and the NSTAR dispenser cathode.**

mechanisms, such as poisoning degrading the work function or impurity build-up plugging the pores, actually cause the cathode life limit. Likewise, recycling of the barium will extend the dispenser cathode life, so uncertainties in the dispenser cathode life estimates by this model have the same uncertainties due to impurities and redeposition that are found for the $LaB_6$ life model (although $LaB_6$ is less likely to be affected by impurities). Therefore, a direct comparison of calculated life versus discharge current will be made with the understanding that the curves will likely shift together vertically due to impurity or redeposition issues. The $LaB_6$ cathode life is projected to exceed the dispenser cathode life by nearly an order of magnitude at the nominal NSTAR full-power currents of less than 15 A. If the NSTAR cathode is capable of producing higher discharge currents than 15 A, the $LaB_6$ cathode life is still projected to exceed the NSTAR life over the full current range demonstrated by the $LaB_6$ cathode. As shown in Fig. 6-47, the larger $LaB_6$ cathodes will have even longer lifetimes, and their life significantly exceeds that projected for the NEXIS 1.5-cm-diameter dispenser cathode [47] that is designed to operate up to about 35 A.

## 6.8.5  Cathode Poisoning

Comprehensive investigations of the poisoning of dispenser cathodes [17] and $LaB_6$ cathodes [55] have been published in the literature. The most potent poisons for both cathodes are oxygen and water, with other gases such as $CO_2$ and air producing poisoning effects at higher partial pressures. Figure 6-49 shows the reduction percentage of the electron emission current density in
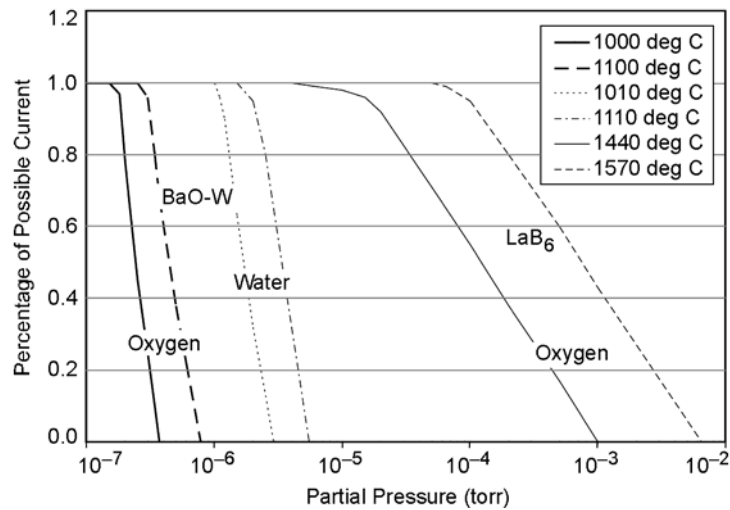
**Fig. 6-49. Percentage of possible thermionic emission versus partial pressure of oxygen and water, showing the sensitivity of dispenser cathodes relative to LaB$_6$ (from [18]).**

diode tests of a Type S 4:1:1 dispenser cathode and a LaB$_6$ cathode as a function of the partial pressures of oxygen and water for two different emitter temperatures. Oxygen partial pressures in the $10^{-7}$-torr range can completely poison the dispenser cathode at temperatures of 1100˚C. In a similar manner, water vapor at partial pressures in the $10^{-6}$-torr range will poison dispenser cathodes at temperatures below 1110˚C. For typical pressures inside hollow cathodes in excess of 1 torr, partial pressures in this range represent the best purity level that can be achieved by the gas suppliers, resulting in the high "propulsion-grade" purity mentioned above. This is the reason for the stringent purity requirement levied on conventional dispenser hollow cathodes in the U.S. to date. Recent experiments by Polk [56] showed that oxygen poisoning observed in vacuum devices occurred only in hollow cathodes at low plasma densities (low current) and high oxygen levels (>10 PPM), and that the plasma environment inside hollow cathodes tended to mitigate the poisoning of oxygen in dispenser cathodes. However, the plasma may aid in the formation of volatile tungsten oxides and tungstates from the impurity gases that contribute to tungsten migration and redeposition on the insert surface. This modifies the dispenser cathode surface morphology, which may affect the emission capabilities. It is likely that the life of dispenser cathodes can be degraded to some extent by propellant impurities, which has yet to be fully identified and quantified.

Lanthanum hexaboride is much less sensitive to impurities that can limit the performance and life of the barium dispenser cathodes. Partial pressures of

oxygen in the $10^{-5}$-torr range are required to degrade the emission of $LaB_6$ at temperatures below 1440°C, which is shown in Fig. 6-49. The curves for water and air poisoning of $LaB_6$ are at much higher partial pressures off the graph to the right. In comparison, $LaB_6$ at 1570°C, where the electron emission current density is nearly the same as for the dispenser cathode at 1100°C, can withstand oxygen partial pressures up to $10^{-4}$ torr without degradation in the electron emission. This means that $LaB_6$ can tolerate impurity levels in the feed gas two orders of magnitude higher as compared with dispenser cathodes operating at the same emission current density. For the case of xenon ion thrusters, $LaB_6$ cathodes can tolerate the crudest grade of xenon available (≈99.99% purity) without affecting the $LaB_6$ electron emission or life. $LaB_6$ cathodes also do not require any significant conditioning or activation procedures that are required by dispenser cathodes. The authors have used $LaB_6$ cathodes emitting at currents of 5 to 10 A/cm$^2$ to produce pure oxygen plasmas in background pressures of $10^{-3}$ torr of oxygen. In this case, the operating temperature of the cathode had to be increased to just over 1600°C to avoid poisoning of the surface by the formation of lanthanum oxide, consistent with the trends in the published poisoning results shown in Fig. 6-49. The authors have also exposed hot, operating $LaB_6$ cathodes to atmospheric pressures of both air and water vapor. In both cases, the system was then pumped out, the heater turned back on, and the cathodes started up normally. This incredible robustness makes handling and processing electric propulsion devices that use $LaB_6$ cathodes significantly easier than thrusters that use dispenser cathodes.

## 6.9  Keeper Wear and Life

The keeper electrode typically encloses the hollow cathode and serves the functions of facilitating the starting of the cathode by bring a high positive voltage close to the orifice and protecting the cathode from ion bombardment from the cathode plume and thruster plasmas. However, the keeper electrode is biased during normal operation at an intermediate potential between cathode and anode to collect a reduced number of electrons, and since it is below the plasma potential, it is subject to ion bombardment and wear. Cathode orifice plate and keeper electrode erosion rates measured or inferred in various experiments [57,58] and in ion thruster life tests [34,53,59] have been found to be much higher than anticipated. For example, Fig. 6-50 shows the NSTAR cathode before and after the 30,352-hour extended life test [38]. The keeper electrode was completely eroded away by the end of the test, exposing the cathode orifice plate to the thruster discharge chamber plasma, which significantly eroded the cathode orifice plate and the sheath-heater surfaces. These results have been attributed to the high-energy ions bombarding and sputtering the cathode and keeper electrodes.
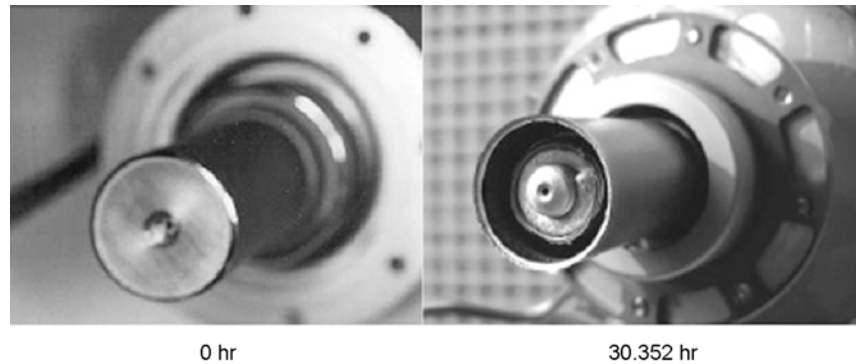
0 hr                                                                   30.352 hr

**Fig. 6-50. NSTAR discharge cathode before and after the ELT wear test, showing complete sputter erosion of the keeper electrode [38].**

A significant effort has been expended trying to understand the mechanism for this rapid erosion. Several organizations have measured the presence of high-energy ions in ion thrusters and in the neighborhood of hollow cathodes using retarding potential analyzers (RPAs) [46,60,61] and laser-induced fluorescence (LIF) [62]. For example, Fig. 6-51 shows the ion energy distribution measured downstream on axis and radially away from the plasma ball for the NSTAR cathode [46]. The high-energy ions are detected in both locations, with varying amounts depending on the position at which they are detected. The energy of some of the ions is greatly in excess of the 26-V discharge voltage, and if these ions were to hit the keeper or cathode orifice, they could cause significant erosion.

The source and characteristics of the high-energy ions have been the subject of much research and debate. Models of a direct current (DC) potential hill [63] located inside or just downstream of the cathode orifice, or ion acoustic instabilities in a double layer postulated in the orifice of the cathode [64], have been proposed to explain the production of these ions. However, in probe studies to date [1,6,28,42], there has been no detectable potential hill or unstable double layer at the cathode orifice or in the cathode plume that might explain the mechanisms responsible for the high-energy ions or the electrode wear rates and erosion patterns. High-frequency plasma potential oscillations in the 50- to 1000-kHz range associated with plasma instabilities have been detected in the cathode plume and across the front of the keeper by scanning emissive probes [46] and have been proposed as a mechanism for accelerating ions to high energy. In this case, ions born at the peak potential gain the full radio frequency (rf) potential energy when striking the keeper or cathode surfaces, which can exceed 40 to 80 eV [46]. The fluctuations then produce sufficient ion energy to explain the keeper-face erosion reported in the literature.
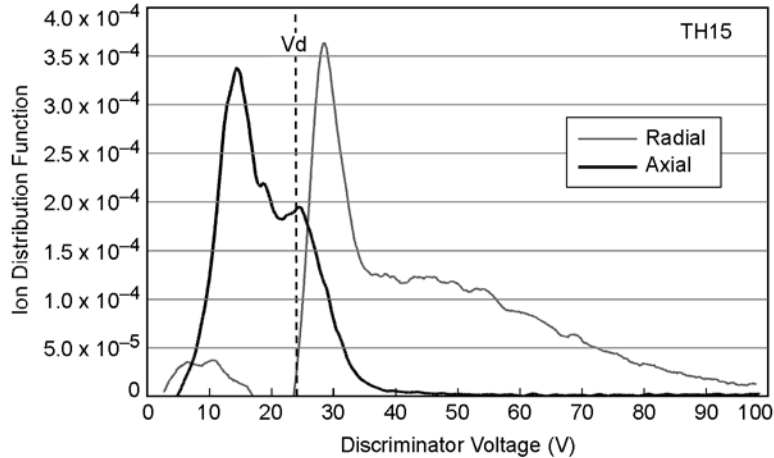
**Fig. 6-51. Ion energy distribution measured on axis and radially away from an NSTAR hollow cathode (from [46]).**

However, the fluctuations measured to date are not of sufficient amplitude to explain the significant number of ions detected by the radially positioned RPA with energies approaching or even exceeding 100 eV. Katz [65] has shown the importance of charge exchange collisions on radially accelerated ions, and how it leads to ions with higher energies than the measured plasma potentials.

Immediately downstream of the discharge cathode keeper the radial plasma potential profile has a substantial dip on axis. Ions generated on the edges of the potential dip are accelerated towards the centerline. The neutral gas density, which is dominated by un-ionized gas coming out of the hollow cathode, also peaks on axis. Near the cathode, the neutral gas density is high enough that a substantial fraction of ions is neutralized by resonant charge exchange with gas atoms before making it across the potential dip. Since they are now neutral, the xenon atoms do not lose the kinetic energy they gained as ions falling into the dip, passing through to the other side of the potential dip. However, as they continue to drift radially some of the atoms are ionized, either by charge exchange or collisions with electrons, and, again, are influenced by the electric fields. By the time these ions reach the RPA, they have their original thermal energy plus the energy they gained falling down the dip, plus the energy from the plasma potential where they were re-ionized. This process is shown schematically in Fig. 6-52. The measured high energies are attained because, as a neutral particle, the xenon atom is not retarded by the potential rise, but gains the potential energy moving through the trough.
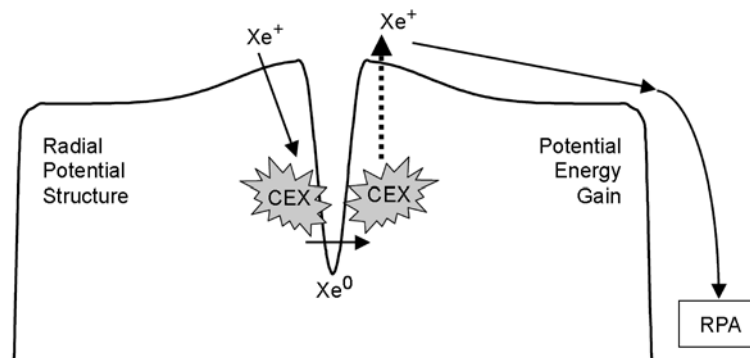
**Fig. 6-52. Xenon ions gain energy falling down the potential well, are charge exchanged, travel past the potential rise without losing energy, and regain their charge in a high potential region [65].**

For example, a calculated spectrum is shown in Fig. 6-53. The primary, non-charge-exchanged ion spectrum was estimated as a Maxwellian distribution with an energy of 3.5 eV, the measured electron temperature. The high-energy ion portion of the spectrum, while somewhat lower than the measurement, shows the same general features. The calculated spectrum has no ions above 95 V, while the measured spectrum shows a few ions above this energy. Katz [65] suggests that these very high-energy ions may have started out as double ions when they entered the axial potential well and picked up twice the kinetic energy prior to being neutralized by charge exchange. The complete mechanisms for high-energy ion generation, the measured energies of these ions by various techniques, and the enhanced erosion of the cathode and keeper electrodes are still under investigation at this time. Detailed 2-D modeling [66] and additional experimental investigations are under way to understand and mitigate this problem.

## 6.10 Hollow Cathode Operation

The electron discharge from hollow cathodes can be initiated by several mechanisms. In Type A cathodes and some Type B with small orifices, the electrostatic (vacuum) potential from the keeper or anode electrode does not penetrate significantly through the relatively long, thin orifice into the insert region. In this case, electrons emitted in the insert region cannot be accelerated to cause ionization because there is no anode potential visible inside the cathode. However, if the cathode uses a barium dispenser insert, then barium evaporated from the insert when heated can deposit on the upstream side of the cathode orifice plate and inside the orifice and diffuse onto the downstream surface of the orifice plate [67] facing the keeper electrode. The work function subsequently decreases, and the vacuum thermionic emission from the orifice
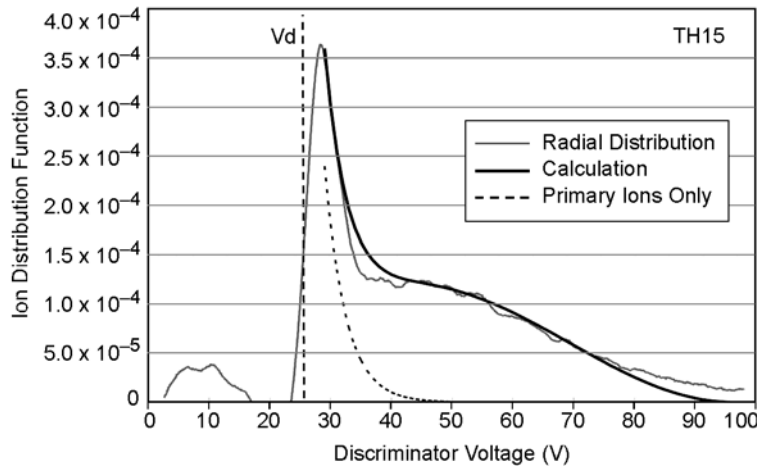
**Fig. 6-53. The xenon ions gain most of their kinetic energy in the sheath and the potential well on axis (from [65]).**

plate to the keeper can be sufficient to ignite a discharge once gas is introduced. The plasma then penetrates the orifice, extending the anode potential into the insert region and the discharge transitions directly to the insert. The orifice plate is subject to sputter erosion by the ions in the discharge, and the barium layer is removed and has to be reestablished if the cathode is turned off in order to restart [68].

For cathodes with larger orifices (typically 2-mm diameter or larger), a sufficient keeper voltage (typically 100 to 500 V) will cause the applied positive potential to penetrate inside the insert region with levels in excess of the ionization potential of the propellant gas. The electrons from the insert then can be accelerated locally inside the insert and cause ionization, which ignites the discharge through the orifice to the keeper or anode. This is the mechanism used in most of the $LaB_6$ cathodes developed by the authors to strike the discharge.

For hollow cathodes with smaller orifices or inhibited orifice-plate emission (due to surface impurities, barium depletion, etc.), an arc-initiation technique typically is used. In this case, the applied keeper voltage is pulsed to a high positive value (typically >500 V). The discharge starts due to either field emission of electrons from the orifice plate ionizing the injected cathode gas or Paschen breakdown occurring at the relatively high pressure in the cathode-to-keeper gap generating plasma that penetrates the orifice into the insert region. To ensure reliable thruster ignition over life, it is standard to apply both a DC keeper voltage in the 50- to 150-V range and a pulsed keeper voltage in the

300- to 600-V range. Once the discharge is ignited, the keeper current is limited by the power supply and the voltage falls to a low value below the discharge voltage.

Once ignited, hollow cathodes are well known to operate in distinct discharge "modes." In ion thrusters, the hollow cathode discharge operation has been historically characterized as having a quiescent "spot mode" with a broadly optimum gas flow at a given current, and a noisy "plume mode" with the gas flow below the level at which the spot mode is obtained [44,45]. The spot mode, seen in Fig. 6-28(a), is visually observed as manifesting a ball or "spot" of plasma just downstream of the cathode orifice with little visual glow from the downstream plasma at low currents and a slowly expanding plasma column extending from the spot into the thruster discharge chamber at higher currents. The plume mode is seen visually as a widely diverging plasma cone extending from the cathode, often filling the vacuum chamber with diffuse plasma and little or no spot or ball of plasma in the cathode/keeper orifice. There is a continuous transition between these modes, which is sometime separately identified as a transition mode [3]. A less well-known third mode, sometimes called a "stream mode," occurs at high gas flows well above the optimum for the spot mode. In this stream mode, shown just starting in Fig. 6-28(b), the plasma spot is pushed well down stream of the cathode/keeper orifice, and a dark space between the cathode or keeper electrode and the spot is usually observed. In this case, the plasma expands and disperses faster than in the normal spot mode. Very high cathode flow rates tend to suppress the discharge voltage, which adversely affects the ionization rate and discharge performance in discharge cathodes in ion thrusters. However, higher flow rates tend to reduce the coupling voltage in both Hall and ion thruster neutralizer cathodes, which can improve the performance.

The hollow cathode discharge modes have been examined in detail due to the observed increases in the keeper or coupling voltages in the plume mode [44,45,64,69,70] and increases in keeper wear [53,69]. At flow rates near the optimum for the spot mode, thermionic hollow cathodes can produce quiescent discharges [46,64]. In neutralizer cathodes, transition to plume mode occurs when too low a gas flow rate and/or keeper current is provided for the desired emission current. Plume mode transition is usually detected by increases in the oscillation of the keeper voltage or in the magnitude of the coupling voltage. For example, plume mode onset is defined in the NSTAR neutralizer when the keeper voltage oscillation exceeds 5 V [71]. In discharge cathodes, transition to plume mode also occurs for too low a propellant flow at a given emission current (or too high a discharge current for a given flow), and is usually detected by increases in the discharge voltage oscillations. Transition to plume mode usually occurs at higher emission current densities (related to the size of

the orifice and the discharge current) and can be affected by the anode location and design [46].

As the discharge current is increased for a given cathode orifice size and gas flow rate, the noise in the discharge voltage and in probe signals from the plasma increases [70], and the cathodes produce ions with energies significantly in excess of the discharge voltage and produce significant keeper and cathode orifice erosion. This leads to the keeper and cathode life issues discussed above associated with plume-mode behavior and often determines the cathode geometry and operation conditions selected for any given thruster.

Figure 6-54 shows the discharge voltage versus current for a 1.5-cm-diameter dispenser hollow cathode with a 2.1-mm orifice for several different flow rates [6]. In this case, two different anode geometries were used: one was a 45-deg conical anode and the second was a 5-cm-diameter cylindrical anode. The maximum current in the plot that could be achieved at a given gas flow was due to the onset of strong discharge voltage oscillations of greater than ±5 V. The small cylindrical anode permitted significantly higher discharge currents to be obtained before the oscillation limits and also reduced the discharge voltage at all currents. This is due to the increased gas pressure near the cathode exit increasing the plasma generation in the cathode plume, which could only be achieved with the conical anode by injecting significant amounts of gas directly into the anode region. It is clear that the onset of the oscillations and the transition to plume mode is an anode-plasma effect, which will be discussed further later.
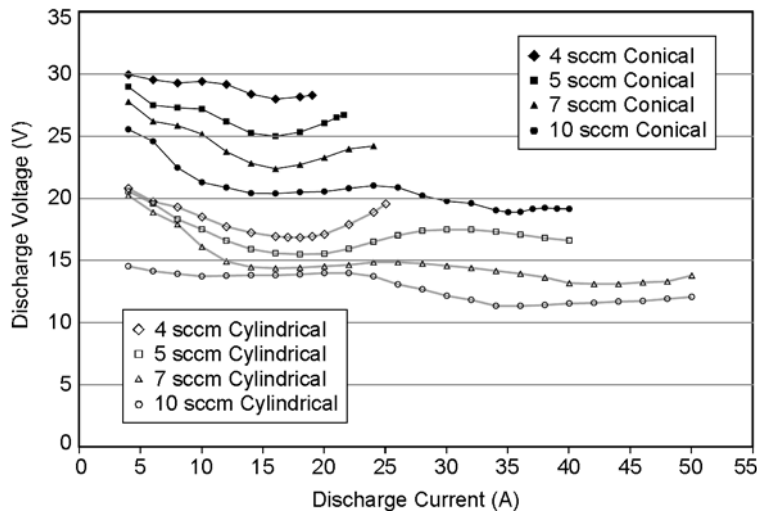


**Fig. 6-54. Discharge voltage versus current for several hollow
cathode flow rates for two anode configurations.**

There are basically three types of oscillations that occur in hollow cathode discharges [46,70]. First, there are plasma discharge oscillations in the frequency range of 50 to over 1000 kHz. These are usually incoherent oscillations in the ion acoustic frequency range with amplitudes that vary continuously from fractions of a volt on the electrodes in the spot mode to tens of volts on the electrodes into the plume mode. If sufficiently large, these ion acoustic oscillations can trigger regulation problems in the power supply, leading to large discharge voltage oscillations on power-supply-regulation times of 100 to 1000 Hz. This behavior is shown in Fig. 6-55.

As the discharge current increases, the ionization percentage in the cathode plume becomes significant and can lead to ionization instabilities or so-called *predator–prey* oscillations. In this case, the plasma discharge burns out a significant fraction of the neutral gas, and the discharge collapses on the time frame of neutral flow into the plume region. The frequency range of these instabilities is in the 50- to 250-kHz range for xenon, depending on the physical scale lengths and size of the discharge components. Ionization instabilities are easily observed in the plasma density, which is shown by the probe's ion saturation current oscillations in Fig. 6-56 and compared to the normally observed oscillations from the incoherent ion acoustic-type modes. Ionization instabilities usually can be inhibited by proper selection of the gas flow and/or magnitude of any applied axial magnetic field in the cathode plume region [46], which modifies the local ion generation rate.
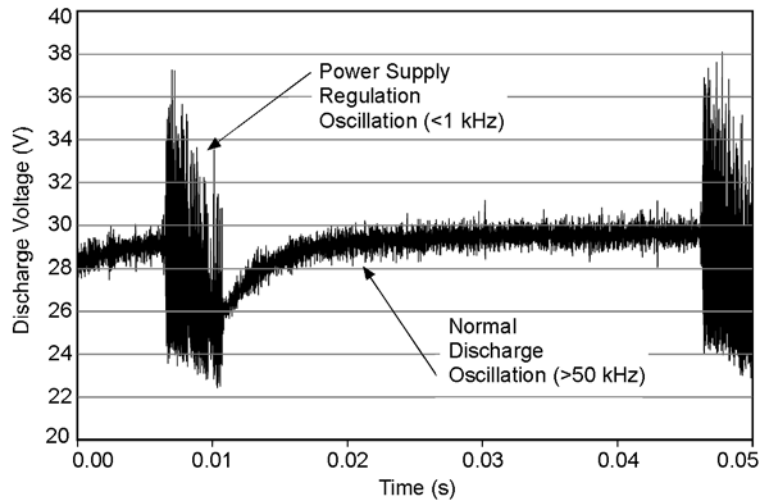


**Fig. 6-55. Discharge voltage oscillations showing plasma and power supply oscillations.**

It is important to realize that the large discharge oscillations and transition to plume mode is an effect that occurs exterior to the hollow cathode [70]. Figure 6-57 shows the ion saturation current measured inside the insert region and immediately outside the keeper in the above experiments during the ionization instability conditions. The plasma density oscillations inside the cathode insert plasma are small in amplitude and uncorrelated to the ionization and large turbulent instabilities observed outside in the keeper plasma region. The higher gas flows injected to avoid transition to plume mode are required to
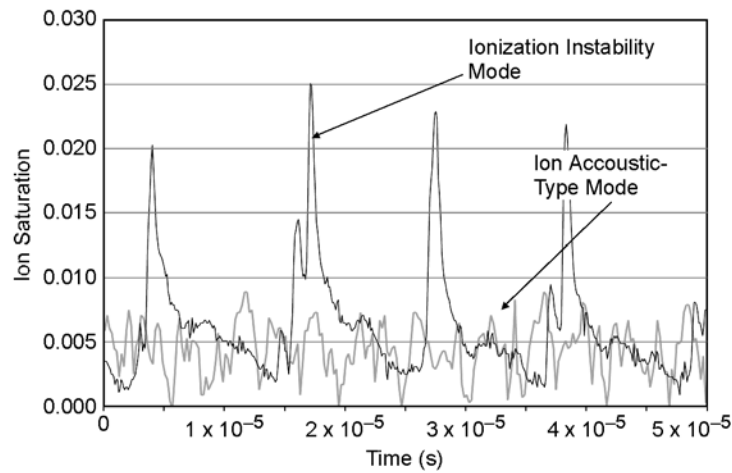


**Fig. 6-56. Discharge voltage oscillations showing plasma plume mode oscillations with frequencies in >100-kHz range and ionization-related oscillations in the <100-kHz range.**
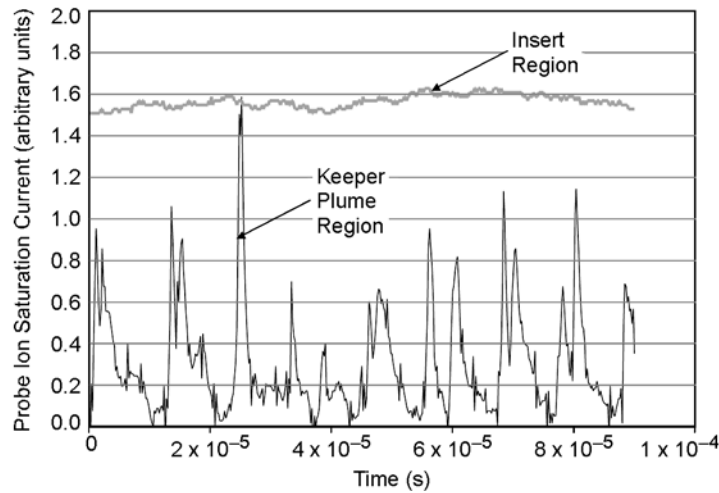


**Fig. 6-57. Ion saturation current oscillations inside and outside the cathode, showing oscillation location.**

produce sufficient plasma density to carry the discharge current, and the lower electron temperatures and collisional effects in the cathode plume plasma tend to damp or extinguish the oscillations. This oscillatory and damping behavior is suggested by the cathode plume models [39,41,72,73] in the literature and discussed above.

# References

[1]    D. M. Goebel, K. Jameson, I. Katz, and I. Mikellades, "Hollow Cathode Theory and Modeling: I. Plasma Characterization with Miniature Fast-Scanning Probes," *Journal of Applied Physics*, vol. 98, no. 10, 113302, 2005.

[2]    I. Mikellades, I. Katz, D. M. Goebel, and K. K. Jameson, "Plasma Processes Inside Orificed Hollow Cathodes," *Physics of Plasmas*, vol. 13, 063504, 2006.

[3]    H. R. Kaufman, "Technology of Electron-Bombardment Ion Thrusters," *Advances in Electronics and Electron Physics*, vol. 36, edited by L. Marton, New York: Academic Press, 1974.

[4]    B. A. Arkhopov and K. N. Kozubsky, "The Development of the Cathode Compensators for Stationary Plasma Thrusters in the USSR," 22nd International Electric Propulsion Conference, paper IEPC-91-023, Viareggio, Italy, October 14–17, 1991.

[5]    I. Mikellades, I. Katz, D. M. Goebel, and K. K. Jameson, "Hollow Cathode Theory and Modeling: II. A Two-Dimensional Model of the Emitter Region," *Journal of Applied Physics*, vol. 98, no. 10, 113303, 2005.

[6]    D. M. Goebel, K. Jameson, R. Watkins, and I. Katz, "Cathode and Keeper Plasma Measurements Using an Ultra-Fast Miniature Scanning Probe," AIAA-2004-3430, 40th Joint Propulsion Conference, Ft. Lauderdale, Florida, July 11–14, 2004.

[7]    O. W. Richardson, "Electron Theory of Matter," *Philips Magazine*, vol. 23, pp. 594–627, 1912.

[8]    W. H. Kohl, *Handbook of Materials and Techniques for Vacuum Devices*, New York: Reinhold, 1967.

[9]    W. Schottky, "Concerning the Discharge of Electrons from Hot Wires with Delayed Potential," *Annalen der Physik*, vol. 44, no. 15, pp, 1011–1032, July 1914.

[10]   A. T. Forrester, *Large Ion Beams*, New York: Wiley-Interscience, 1988.

[11]  J. W. Gibson, G. A. Haas, and R. E. Thomas, "Investigation of Scandate Cathodes: Emission, Fabrication and Activation Processes," *IEEE Transactions on Electron Devices*, vol. 36, pp. 209–214, 1989.

[12]  J. L. Cronin, "Modern Dispenser Cathodes," IEE Proceedings, vol. 128, no. 19, 1981.

[13]  J. M. Lafferty, "Boride Cathodes," *Journal of Applied Physics*, vol. 22, p. 299, 1951.

[14]  D. Jacobson and E. K. Storms, "Work Function Measurement of Lanthanum-Boron Compounds," *IEEE Transactions on Plasma Science*, vol. 6, pp. 191–199, 1978.

[15]  E. Storms and B. Mueller, "A Study of Surface Stoichiometry and Thermionic Emission using LaB6," *Journal of Applied Physics*, vol. 50, pp. 3691–3698, 1979.

[16]  R. Levi, "Improved Impregnated Cathode," *Journal of Applied Physics*, vol. 26, p. 639, 1955.

[17]  J. L. Cronin, "Practical Aspects of Modern Dispenser Cathodes," *Microwave Journal*, vol. 22, pp. 57–62, September 1979.

[18]  D. M. Goebel, R. M. Watkins, and K. K. Jameson, "LaB6 Hollow Cathodes for Ion and Hall Thrusters," *Journal of Propulsion and Power*, vol. 23, no. 3, pp.552–558, 2007.

[19]  J. Pelletier and C. Pomot, "Work Function of Sintered Lanthanum Hexaboride," *Applied Physics Letters*, vol. 34, pp. 249–251, 1979.

[20]  V. Kim, G. Popov, B. Arkhipov, V. Murashko, O. Gorshkov, A. Koroteyev, V. Garkusha, A. Semenkin, and S. Tverdokhlebov, "Electric Propulsion Activity in Russia," IEPC-2001-005, 27th International Electric Propulsion Conference, Pasadena, California, October 14–19, 2001.

[21]  D. M. Goebel, J. T. Crow, and A. T. Forrester, "Lanthanum Hexaboride Hollow Cathode for Dense Plasma Production," *Review of Scientific Instruments*, vol. 49, pp. 469–472, 1978.

[22]  D. M. Goebel, Y. Hirooka, and T. Sketchley, "Large Area Lanthanum Hexaboride Electron Emitter," *Review of Scientific Instruments*, vol. 56, pp. 1717–1722, 1985.

[23]  E. Storms and B. Mueller, "Phase Relationship, Vaporization and Thermodynamic Properties of the Lanthanum-Boron System," *Journal of Chemical Physics*, vol. 82, p. 51, 1978.

[24]  K. N. Leung, P. A. Pincosy, and K. W. Ehlers, "Directly Heated Lanthanum Hexaboride Filaments," *Review of Scientific Instruments*, vol. 55, pp. 1064–1068, 1984.

[25] I. Katz, J. Anderson, J. Polk, and D. M. Goebel, "Model of Hollow Cathode Operation and Life Limiting Mechanisms," IEPC-2003-0243, 28th International Electric Propulsion Conference, Toulouse, France, March 17–21, 2003.

[26] I. Katz, J. Anderson, J. Polk, and J. Brophy, "One Dimensional Hollow Cathode Model," *Journal of Propulsion and Power*, vol. 19, no. 4, pp. 595–600, 2003.

[27] J. S. Miller, S. H. Pullins, D. J. Levandier, Y. Chiu, and R. A. Dressler, "Xenon Charge Exchange Cross Sections for Electrostatic Thruster Models," *Journal of Applied Physics*, vol. 91, no. 3, pp. 984–991, 2002.

[28] K. Jameson, D. M. Goebel, and R. Watkins, "Hollow Cathode and Thruster Discharge Chamber Plasma Measurements Using High-Speed Scanning Probes," IEPC-2005-269, 29th International Electric Propulsion Conference, Princeton University, Princeton, New Jersey, October 31– November 4, 2005.

[29] D. L. Book, *NRL Plasma Formulary*, Naval Research Laboratory, Washington, D.C., 1987.

[30] I. Katz, J. Polk, I. Mikellides, D. M. Goebel, and S. Hornbeck, "Combined Plasma and Thermal Hollow Cathode Insert Model," IEPC-2005-228, 29th International Electric Propulsion Conference, Princeton University, Princeton, New Jersey, October 31–November 4, 2005.

[31] K. Jameson, D. M. Goebel, and R. Watkins, "Hollow Cathode and Keeper Region Plasma Measurements," AIAA-2005-3667, 41st Joint Propulsion Conference, Tucson, Arizona, July 11–14, 2005.

[32] I. Mikelides, I. Katz, D. M. Goebel, and J. Polk, "Theoretical Model of a Hollow Cathode Plasma for the Assessment of Insert and Keeper Lifetimes," AIAA-2005-4234, 41st Joint Propulsion Conference, Tucson, Arizona, July 2005.

[33] J. E. Polk, A. Grubisic, N. Taheri, D. M. Goebel, R. Downey, and S. Hornbeck, "Emitter Temperature Distributions in the NSTAR Discharge Hollow Cathode," AIAA-2005-4398, 41st Joint Propulsion Conference, Tucson, Arizona, July 11–14, 2005.

[34] J. E. Polk, J. R. Anderson, J. R. Brophy, V. K. Rawlin, M. J. Patterson, J. S. Sovey, and J. J. Hamley, "An Overview of the Results from an 8200-Hour Wear Test of the NSTAR Ion Thruster," AIAA Paper 99-2446, 35th Joint Propulsion Conference, Los Angeles, California, June 20–24, 1999.

[35] I. Katz, J. Anderson, J. Polk, and J. Brophy, "A Model of Hollow Cathode Plasma Chemistry," AIAA-2002-4241, 38th Joint Propulsion Conference, Indianapolis, Indiana, July 7–10, 2002.

[36] J. G. Andrews and J. E. Allen, "Theory of a Double Sheath Between Two Plasmas," *Proceedings of the Royal Society of London*, Series A, vol. 320, p. 459–472, 1971.

[37] V. Rawlins, J. S. Sovey, J. R. Anderson, and J. E. Polk, "NSTAR Flight Thruster Qualification Testing," AIAA-98-3936, 34th Joint Propulsion Conference, Cleveland, Ohio, July 13–15, 1998.

[38] A. Sengupta, J. R. Brophy, and K. D. Goodfellow. "Status of The Extended Life Test of The Deep Space 1 Flight Spare Ion Engine After 30,352 Hours of Operation," AIAA Paper 2003-4558, 39th Joint Propulsion Conference, Huntsville, Alabama, July 20–23, 2003.

[39] I. Katz, I. G. Mikellides, and D. M. Goebel, "Model of the Plasma Potential Distribution in the Plume of a Hollow Cathode," AIAA Paper 2004-4108, 40th Joint Propulsion Conference, Ft. Lauderdale, Florida, July 11–14, 2004.

[40] I. Langmuir, "The Interaction of Electron and Positive Ion Space Charges in Cathode Sheaths," *Physical Review*, vol. 33, no. 6, pp. 954–989, 1929.

[41] I. G. Mikellides, I. Katz, D. M. Goebel, and K. K. Jameson, "Towards the Identification of the Keeper Erosion Mechanisms: 2-D Theoretical Model of the Hollow Cathode," AIAA-2006-5151, 42nd Joint Propulsion Conference, Sacramento, California, July 10–13, 2006.

[42] D. A. Herman and A. D. Gallimore, "Near Discharge Cathode Assembly Plasma Potential Measurements in a 30-cm NSTAR Type Ion Engine Amidst Beam Extraction," AIAA-2004-3958, 40th Joint Propulsion Conference, Ft. Lauderdale, Florida, July 11–14, 2004.

[43] K. K. Jameson, D. M. Goebel, I. G. Mikellides, and R. M. Watkins, "Local Neutral Density and Plasma Parameter Measurements in a Hollow Cathode Plume," AIAA-2006-4490, 42nd Joint Propulsion Conference, Sacramento, California, July 10–13, 2006.

[44] G. A. Csiky, "Investigation of a Hollow Cathode Discharge Plasma," AIAA-69-258, 7th Electric Propulsion Conference, Williamsburg, Virginia, March 3–5, 1969.

[45] V. K. Rawlin and E. V. Pawlik, "A Mercury Plasma-Bridge Neutralizer," AIAA-67-670, AIAA Electric Propulsion and Plasmadynamics Conference, Colorado Springs, Colorado, September 11–13, 1967.

[46] D. M. Goebel, K. Jameson, I. Katz, I. Mikellides, and J. Polk, "Energetic Ion Production and Keeper Erosion in Hollow Cathode Discharges," IEPC-2005-266, 29th International Electric Propulsion Conference, Princeton University, Princeton, New Jersey, October 31–November 4, 2005.

[47] D. M. Goebel, I. Katz, Y. Mikellides, and J. Polk, "Extending Hollow Cathode Life for Deep Space Missions," AIAA-2004-5911, AIAA Space 2004 Conference, San Diego, California, September 2004.

[48] R. Doerner, G. Tynan, D. M. Goebel, and I. Katz, "Plasma Surface Interaction Studies for Next-Generation Ion Thrusters," AIAA-2004-4104, 40th Joint Propulsion Conference, Ft. Lauderdale, Florida, July 2004.

[49] R. P. Doerner, S. I. Krasheninnikov, and K. Schmidt, "Particle-Induced Erosion of Materials at Elevated Temperature," *Journal of Applied Physics*, vol. 95, no. 8, pp. 4471–4475, 2004.

[50] J. E. Polk, C. Marrese, B. Thornber, L. Dang, and L. Johnson, "Temperature Distributions in Hollow Cathode Emitters," AIAA-2004-4116, 40th Joint Propulsion Conference, Ft. Lauderdale, Florida, July 11–14, 2004.

[51] P. Palluel and A. M. Shroff, "Experimental Study of Impregnated-Cathode Behavior, Emission, and Life," *Journal of Applied Physics*, vol. 51, no. 5, pp. 2894–2902, 1980.

[52] T. R. Sarver-Verhey, "28,000 Hour Xenon Hollow Cathode Life Test Results," IEPC-97-168, 25th International Electric Propulsion Conference, Cleveland, Ohio, August 24–28, 1997.

[53] A. Sengupta, J. R. Brophy, J. R. Anderson, and C. Garner. "An Overview of the Results from the 30,000 Hour Life Test of The Deep Space 1 Flight Spare Ion Engine," AIAA Paper 2004-3608, 40th Joint Propulsion Conference, Ft. Lauderdale, Florida, July 11–14, 2004.

[54] J. E. Polk, D. M. Goebel, J. S. Snyder, and A. C. Schneider, "Performance and Wear Test Results for a 20-kW Class Ion Engine with Carbon-Carbon Grids," AIAA_2005-4393, 41st Joint Propulsion Conference, Tucson, Arizona, July 11–14, 2005.

[55] H. E. Gallagher, "Poisoning of LaB6 cathodes," *Journal of Applied Physics*, vol. 40, pp. 44–51, 1969.

[56] J. E. Polk, "The Effect of Reactive Gases on Hollow Cathode Operation," AIAA-2006-5153, 42nd Joint Propulsion Conference, Sacramento, California, July 9–12, 2006.

[57] R. D. Kolasinski and J. E. Polk, "Characterization of Cathode Keeper Wear By Surface Layer Activation," AIAA Paper 2003-5144, 39th Joint Propulsion Conference, Huntsville, Alabama, July 20–23, 2003.

[58] M. Domonkos, J. Foster, and G. Soulas, "Wear Testing and Analysis of Ion Engine Discharge Cathode Keeper," *Journal of Propulsion and Power*, vol. 21, pp. 102–110, 2005.

[59] M. J. Patterson, V. K. Rawlin, J. S. Sovey, M. J. Kussmaul, and J. Parkes, "2.3 kW Ion Thruster Wear Test," AIAA-95-2516, 31st Joint Propulsion Conference, San Diego, California, July 10–12, 1995.

[60] I. Kameyama and P. J. Wilbur, "Measurement of Ions from High Current Hollow Cathodes Using Electrostatic Energy Analyzer," *Journal of Propulsion and Power*, vol. 16, p. 529, 2000.

[61] C. Farnell and J. Williams, "Characteristics of Energetic Ions from Hollow Cathodes," IEPC Paper 03-072, 28th International Electric Propulsion Conference, Toulouse, France, March 17–21, 2003.

[62] G. Williams, Jr., T. B. Smith, M. T. Domonkos, A. D. Gallimore, and R. P. Drake, "Laser Induced Fluorescence Characterization of Ions Emitted from Hollow Cathodes," *IEEE Transactions on Plasma Science*, vol. 28, issue 5, pp. 1664–1675, 2000.

[63] I. Kameyama and P. J. Wilbur, "Potential-Hill Model of High-Energy Ion Production near High Current Hollow Cathodes," ISTS 98-a-2-17, 21st International Symposium on Space Technology and Science, Sonic City, Omiya, Japan, May 1998.

[64] V. J. Friedly and P. J. Wilbur, "High Current Hollow Cathode Phenomena," *Journal of Propulsion and Power*, vol. 8, no. 3, pp. 635–643, 1992.

[65] I. Katz, I. G. Mikellides, D. M. Goebel, K. K. Jameson, and J. E. Polk, "Production of High Energy Ions Near an Ion Thruster Discharge Hollow Cathode," AIAA-2006-4485, 42nd Joint Propulsion Conference, Sacramento, California, July 10–13, 2006.

[66] I. G. Mikellides, I. Katz, and D. Goebel, "Partially-Ionized Gas and Associated Wear in Electron Sources for Ion Propulsion, II: Discharge Hollow Cathode," AIAA-2007-5192, 43rd Joint Propulsion Conference, Cincinnati, Ohio, July 8–11, 2007.

[67] W. G. Tighe, K. Chien, D. M. Goebel, and R. T. Longo, "Hollow Cathode Ignition and Life Model," AIAA-2005-3666, 41st Joint Propulsion Conference, Tucson, Arizona, July 11–14, 2005.

[68] W. Tighe, K. Chien, D. M. Goebel, and R. Longo, "Hollow Cathode Ignition Studies and Model Development," IEPC-2005-314, 29th International Electric Propulsion Conference, Princeton University, Princeton, New Jersey, October 31–November 4, 2005.

[69] J. R. Brophy and C. E. Garner, "Tests of High Current Hollow Cathodes for Ion Engines," AIAA-88-2913, 24th Joint Propulsion Conference, Boston, Massachusetts, July 11–13, 1988.

[70] D. M. Goebel, K. Jameson, I. Katz, and I. Mikellides, "Plasma Potential Behavior and Plume Mode Transitions in Hollow Cathode Discharge," IEPC-2007-027, 30th International Electric Propulsion Conference, Florence, Italy, September 17–20, 2007.

[71] J. R. Brophy, D. E. Brinza, J. E. Polk, M. D. Henry, and A. Sengupta, "The DSI Hyper-Extended Mission," AIAA-2002-3673, 38th Joint Propulsion Conference, Indianapolis, Indiana, July 7–10, 2002.

[72] I. D. Boyd and M. W. Crofton, "Modeling the Plasma Plume of a Hollow Cathode," *Journal of Applied Physics*, vol. 95, pp. 3285–3296, 2004.

[73] I. Mikellides, I. Katz, and D. M. Goebel, "Numerical Simulation of the Hollow Cathode Discharge Plasma Dynamics," IEPC-2005-200, 29th International Electric Propulsion Conference, Princeton University, Princeton, New Jersey, October 31–November 4, 2005.

# Homework Problems

1. The power radiated from a surface is given by $P = \sigma \varepsilon T^4 A$, where $\sigma$ is the Stephan–Boltzmann constant, $\varepsilon$ is the emissivity of the surface, $T$ is the surface temperature in K, and $A$ is the radiating area.

   a. Design a 0.5-mm-diameter tungsten filament electron emitter that emits 10 A and radiates only 200 W of power. Specifically, what is the filament length and emission current density? You can neglect axial conduction of power to the electrical connections and assume that the emissivity of tungsten is 0.3 at emission temperatures.

   b. You decide to use a 0.25-mm-diameter and 4-cm-long filament to limit the radiated power. What is the temperature of the emitter, and how much power is actually radiated?

2. The insert in a BaO hollow cathode has a 3-mm inside diameter, is 2.5-cm long, and is at a temperature of 1100˚C.

   a. Using Cronin's expression for the work function, how much current is emitted by the insert?

   b. If the insert has a uniform plasma with $n_e = 10^{20}$ m$^{-3}$ density and $T_e = 2$ eV inside of it, how much is the electron emission enhanced by the Schottky effect if the sheath is 10 V and 3 Debye lengths thick? What is the total emission current?

   c. Is the emission current space charge limited?

     d. Assume that the plasma density falls exponentially from the orifice entrance to $10^{18}\,\mathrm{m}^{-3}$ in 1 cm. What is the total electron current that can be emitted into the plasma?

3. A 2.5-cm-long BaO-impregnated insert with a 2-cm inside diameter has xenon gas injected to create an internal pressure of 2 torr at 1500 K in the hollow cathode. Assuming the insert plasma is infinitely long, what is the electron temperature in the insert plasma and the radial ion drift velocity at the wall?

4. For the cathode geometry in Chapter 6, Problem 2, what is the internal plasma density for an emission current of 30 A and a heating power of 100 W, assuming a uniform plasma density with an electron temperature of 1.2 eV? (Hint: estimate the resistivity for the sheath voltage, find the plasma density, then iterate.)

5. A lanthanum hexaboride hollow cathode with a 2-cm inside diameter and 2.5-cm long emits 20 A of electrons into a uniform $2\times10^{19}\,\mathrm{m}^{-3}$ plasma with an electron temperature of 1.5 eV. For a heating power of 40 W and an internal xenon pressure of 1.2 torr at 1500 K, find the ion and electron heating powers to the insert. Why is one larger than the other?

6. If a cylindrical discharge cathode orifice is 2 mm in diameter and has an internal pressure of 3 torr at a temperature of 2000 K, what is the electron temperature? (Neglect end losses.)

7. A neutralizer cathode produces 3 A of electron current through a 0.6-mm-diameter orifice that is 1.5-mm long. Assuming that the electron temperature in the orifice is 1.5 eV, the electron temperature in the insert region is 1.2 eV, the pressure is 50 torr at 2000 K, and the sheath voltage at the wall is 12 V, what is the plasma density, the ion heating of the orifice plate, and the axial voltage drop in the orifice plasma?

8. A hollow cathode has an orifice diameter of 2.5 mm and a xenon gas flow of 4 sccm with an effective temperature of 2000 K. Assume that the neutral gas density falls exponentially from the orifice exit with a characteristic length of 0.5 mm (i.e., one *e*-folding for every 0.5 mm of distance from the cathode). Assuming 15-V primary electrons in the cathode plume and that all of the ions generated fall back through the sheath, find the location downstream of the orifice exit where a double layer might occur.

9. A Hall thruster hollow cathode has a cathode orifice diameter of 3 mm and produces 20 A of 15 eV primary electrons with a xenon gas flow of 10 sccm. Assume that the gas is at 2000 K and the neutral plume diverges at 45 deg from the orifice.

   a. Neglecting depletion of the electron current due to ionization, how much of the cathode gas flow is ionized within 10 cm of the cathode?

   b. Assume that every electron that makes an ionization collision is lost (loses most of its energy and is rapidly thermalized) and that the neutral atom is also lost. How much of the cathode gas flow is then ionized within 10 cm of the cathode?

   c. If the primary electron energy is 20 V, how much of the cathode gas flow is ionized within 10 cm of the orifice accounting for both primary electron and neutral gas depletion due to ionization?

10. An ion thruster is operated at 2 A of beam current at 1500 V. The thruster has 5% double ion content, a 10-deg beam divergent half angle, a discharge loss of 160 eV/ion at a discharge voltage of 25 V, and uses 32 sccm of xenon gas and 20 W of power in addition to the discharge power.

    a. What insert thickness is required in an NSTAR-type cathode to achieve 5 years of cathode life if barium loss is the life-limiting effect?

    b. What is the thruster efficiency, Isp, and thrust?